Changes to the Madden-Julian Oscillation with Surface Temperature Warming in Aquaplanet Simulations

Spencer Ressel[a] , Daehyun Kim [ab] , Peter N. Blossey[a]

[a] *University of Washington, Seattle, Washington*

[b] *Seoul National University, Seoul, South Korea*

Corresponding author: Daehyun Kim, daehyun@snu.ac.kr

Current Affiliation: Seoul National University

ABSTRACT: Interactions between waves and the mean-state in the tropics are of fundamental importance for reliable future projection of tropical waves and their impacts under anthropogenic climate change. The Madden-Julian Oscillation (MJO) is the dominant source of weather variability over many parts of the globe on intraseasonal timescales. In this study, we investigate the influence of mean-state changes on the MJO in three aqua-planet experiments made with the Community Atmosphere Model version 6 (CAM6) by prescribing sea surface temperature profiles to capture three different climate states: a current climate-like state, a colder (-4K) state, and a warmer (+4K) state. We find that the MJO strengthens with surface warming, showing higher spectral power over the MJO band (20-100 day period, zonal wavenumbers 1-3) in both circulation and convection fields. Furthermore, MJO-associated precipitation variability increases more strongly than mean-state precipitation with warming, while the east-west ratio increases by a factor of 3x from -4K to +4K. Using a moisture budget approach, two key mechanisms were found to result in MJO strengthening; first, a reduction in the Gross Moist Stability associated with increases in the mean low-level vertical moisture gradient, and second, a reduced damping associated with meridional moisture advection resulting from an increase in the mean low-level meridional moisture gradient. The reduction in GMS is slightly offset, however, by a reduction in the cloud-radiative feedback parameter with warming. This occurs because the cloud top temperature is nearly invariant with warming despite a sharp increase in precipitation.

SIGNIFICANCE STATEMENT: The Madden-Julian Oscillation (MJO) is a global-scale weather system in the tropics that affects weather, particularly rainfall, across the planet. The aim of this study is to improve our understanding of how the MJO may change with future climate change. To do this, we examined model simulations in which the ocean temperature was increased to represent the effects of global warming. Our results suggest that MJO-associated rainfall will become more variable in the future, meaning that 'wet' periods may become wetter and 'dry' periods may become drier. Given the importance of rainfall to agriculture, droughts, and flooding, confident predictions about rainfall in a warmer world are critical for preparatory and adaption work.

1. Introduction

First recognized over 50 years ago, the Madden-Julian Oscillation (MJO; Madden and Julian 1971, 1972) is the preeminent mode of weather variability on intraseasonal timescales in the tropics. Uniquely defined by its slow, eastward propagation and planetary scale, the MJO signal manifests as alternating periods of enhanced and suppressed tropical convection which are coupled to a characteristic 'swallow-tail' circulation pattern associated with a Matsuno-Gill response to heating anomalies (Gill 1980). These wave-like disturbances propagate coherently eastward across the tropics with a phase speed of approximately 5 m s^{-1} in the Warm Pool region of the Indian Ocean and the western Pacific, and a period typically between 20-100 days with the strongest amplitudes occurring in the Warm Pool during boreal winter (Nov.-Apr.) season.

The MJO is a dominant influence on local tropical weather, strongly modulating circulations and rainfall patterns in places like Australia (Wheeler et al. 2009; Marshall et al. 2021), Indonesia (Hidayat and Kizu 2010), and India (Pai et al. 2011) on intraseasonal timescales in addition to modulating tropical Kelvin wave activity in the Indian Ocean (Roundy 2008). Tropical cyclones are also influenced by the MJO, with studies revealing the sensitivity of both tropical cyclogenesis (Maloney and Hartmann 2000a,b; Emlaw and Kim 2024) and tropical cyclone tracks (Klotzbach and Oliver 2015) to MJO phase.

Through its circulation response, the MJO also has an out-sized influence on extra-tropical weather. Studies have found that MJO-associated teleconnections affect weather in North America (Vecchi and Bond 2004; Lorenz and Hartmann 2006; Riddle et al. 2013; Henderson et al. 2016; Tippett 2018), South America (Alvarez et al. 2016; Grimm 2019; Matus et al. 2025), East Asia (Jia et al. 2011; Seo et al. 2016; Kim et al. 2020), and the polar regions (Kang and Tziperman 2018; Lee and Seo 2019). Robust connections have also been shown to exist between the MJO and a variety of low-frequency phenomena such as ENSO (Hendon and Salby 1994; Kessler 2001) and the QBO (Abhik and Hendon 2019; Sakaeda et al. 2020). Due in part to this myriad of teleconnections, the MJO is known to be a leading source of intraseasonal predictability (Waliser et al. 2003; Kim et al. 2014), further motivating research into its behavior and driving mechanisms.

One question of continual importance pertains to the relationship between the MJO and anthropogenic climate change. Several studies have examined changes in MJO behavior between the pre-industrial era (circa 1850) and the present in observations, but sparse data from before the satellite era (pre-1979) results in large uncertainties. One reconstruction of MJO amplitude based on the Real-Time Multivariate MJO (RMM) index of Wheeler and Hendon (2004) suggests that MJO amplitude increased by approximately 13% per century between 1905 and 2018 (Oliver and Thompson 2011), whereas Tao et al. (2015) found no statistically significant trend in boreal winter MJO activity between 1982 and 2009. Given these findings, further research into potential causal relationships between warming and MJO activity is required to both reduce current uncertainty about changes in observed historical MJO activity and to make confident predictions about future changes in MJO activity.

Using Global Climate Models (GCMs) to simulate future warming scenarios, some consistent projections have emerged: in a warmer climate, intraseasonal precipitation and outgoing longwave radiation (OLR) variability are both likely to increase (Subramanian et al. 2014; Wolding et al. 2017; Rushley et al. 2019; Wang et al. 2025), indicative of stronger MJO-associated precipitation anomalies. In a suite of CMIP6 simulations conducted under the Shared Socioeconomic Pathway (SSP) 585 scenario, Wang et al. (2025) found that the multi-model mean MJO-associated precipitation amplitude increased by 17% when comparing the 'projected future' state (2065-2100) to the 'historical' state (1979-2014). However, the models also exhibited significant inter-model spread: while the largest single-model increase was nearly 70%, other models showed weak decreases in MJO-precipitation amplitude with warming. Furthermore, several studies have found that MJO-associated precipitation amplitude increases scale with increases in background power (Rushley et al. 2019) or mean precipitation (Pritchard and Yang 2016), suggesting that changes in

MJO-associated precipitation may result not from dynamical changes in MJO behavior but instead from changes in the model background state.

MJO circulation changes also show inter-model spread. Several studies suggested that MJO-associated 850-hPa zonal wind variance will increase with warming, though to a lesser extent than MJO-associated precipitation anomalies (Subramanian et al. 2014; Rushley et al. 2019; Bui et al. 2023), while other studies find it may decrease slightly (Arnold et al. 2015; Wolding et al. 2017; Bui and Maloney 2018) as mean tropospheric static stability increases. As many MJO teleconnections are mediated by MJO-circulation induced Rossby wave trains, changes to MJO circulation strength have important implications for future intraseasonal predictability (Wolding et al. 2017).

Additionally, no consensus exists regarding the mechanisms responsible for potential changes to MJO characteristics and behavior with warming. Many GCM studies support the notion that moisture advection is critical to MJO strengthening, but some studies emphasize the dominant role of meridional advection (Wang et al. 2025) while others highlight that of vertical advection (Arnold et al. 2013; Arnold and Randall 2015; Wolding et al. 2017). Carlson and Caballero (2016) highlights an alternative mechanism, wherein a transition to super-rotation inhibits eddy activity which itself opposes MJO amplification, resulting in strengthening. Yet another study, Liu (2013), found Wind-Induced Surface Heat Exchange (WISHE) to be a critical process for MJO strengthening.

Compared with full-geography GCM simulations, aqua-planet configurations are reduced complexity models that remove factors such as land-sea contrasts, zonal asymmetries, and other processes shown to be relevant to MJO dynamics such as atmosphere-ocean coupling (DeMott et al. 2015). Though less realistic by construction, such simplifications enable an evaluation of the core mechanisms responsible for MJO behavior and its changes in response to external forcing such as surface warming. To study surface warming-induced changes in MJO characteristics, for example, sea surface temperatures (SSTs) are prescribed as a lower boundary condition, and future warmed states are obtained by prescribing higher SSTs compared to present-day climatology.

Several previous aqua-planet simulations have examined changes to the MJO with warming; using the Community Atmosphere Model v2 (CAM2), Liu (2013) found a strengthening of the MJO with an increase in SSTs from a control run to a +2K SST state and a +4K SST state, manifesting as an increase in intraseasonal precipitation variance. However, changes in 850-hPa zonal wind variance were not spatially uniform, with slight increases over most of the tropics but decreases over equatorial Africa and parts of the Pacific and Central America. In a super-parameterized version of CAM3.5, Arnold et al. (2013) similarly found a strong increase in intraseasonal precipitation variance with surface warming. Using a moist static energy budget approach, they identified increases in the moistening associated with vertical advection as the main mechanism driving MJO amplification. Using SPCAM3.0 Pritchard and Yang (2016) examined a large number of different SST states, ranging from 1°C to 35°C, with globally uniform SST values. Their results highlight both the existence of an MJO signal in very cold climates and the enhancement of MJO activity with surface temperature warming.

This study serves as a continuation of these previous aqua-planet studies, seeking to answer remaining questions about the mechanisms controlling MJO behavior and the behavior of the MJO in both warmer and colder climates.

Specifically, changes to the MJO as a function of sea surface temperature are examined in CAM6 aqua-planet simulations performed by Chien and Kim (2024). Three simulations, representing a control climatology (CTRL) as well as uniformly cooled (-4K SST) and warmed (+4K SST) states, were performed. In that work, a brief description of changes in the mean-state were described and changes in Kelvin wave activity with warming were investigated in detail, but no investigation of MJO activity was performed.

In Section 2, a detailed methodology of the simulations and our analysis is presented. Section 3 presents the results of the simulations, examining changes in both the mean-state and the MJO as a function of SST. Additionally, the results of a moisture budget analysis used to understand the mechanisms driving MJO changes are discussed. Finally, section 4 presents a summary of those results and a conclusion.

2. Methods

In this study we use simulations performed with the Community Atmosphere Model (CAM6) component of second version of the Community Earth System Model (CESM2; Danabasoglu et al. 2020) run in an aqua-planet configuration using the standard ‘QOBS’ zonally-symmetric sea surface temperature profile described in Neale and Hoskins (2000). The horizontal grid has a resolution of 1.9° latitude by 2.5° longitude and the model employs 32 hybrid-sigma coordinate vertical levels. Each simulation was run for a period of 12 years, with the first two years used as a spin-up period and the remaining 10 years used in the analysis. The data were originally output at 3-hourly intervals before being re-sampled to daily for the purposes of studying the MJO, and were interpolated to pressure levels from the native hybrid-sigma vertical coordinate. Additional details about the model configuration can be found in Chien and Kim (2024).

To investigate the influence of mean-state changes on the MJO, three different SST profiles were specified. The control run (CTRL) in which the Neale and Hoskins (2000) profile was used and two perturbed runs in which the SST was everywhere decreased/increased by 4K, termed the '-4K' and '+4K' runs, respectively (Fig. 1). In each experiment the SST profile acts as a proxy for global-scale changes in atmospheric temperature.

Additionally, daily 2.5° longitude and latitude data from the ERA5 dataset are used as a comparison (Hersbach et al. 2020). Mean-state profiles of temperature and specific humidity over the tropical oceans (30°S-30°N) are constructed for winter days (Nov.-Apr.) from 1980-2018. Observations of precipitation are taken from the Tropical Rainfall Measuring Mission (TRMM) for 2001-2014.

a. Regression Analysis

In section 3 we show the results of a regression analysis that was performed to examine the horizontal and vertical structures of the MJO. First, MJO-filtered precipitation was obtained by filtering raw precipitation on intraseasonal timescales (20-100 days) and on MJO spatial scales (zonal wavenumbers 1-3), retaining only eastward propagating signals. Six reference timeseries were then constructed by spatially averaging the MJO-filtered precipitation over 10°x10° boxes centered meridionally on the equator, with each box centered zonally on one of six longitude points equally spaced between 0° and 360°. The fields of interest were regressed onto each timeseries, yielding six sets of regression coefficients at every latitude, longitude, and pressure level. Each set was then shifted in longitude so that its maximum regressed precipitation anomaly occurred at 180° and the six sets were averaged together to produce the final regression coefficients. This procedure was repeated separately for each of the three experiments. A t-test was performed to identify locations with statistically significant regression coefficients.

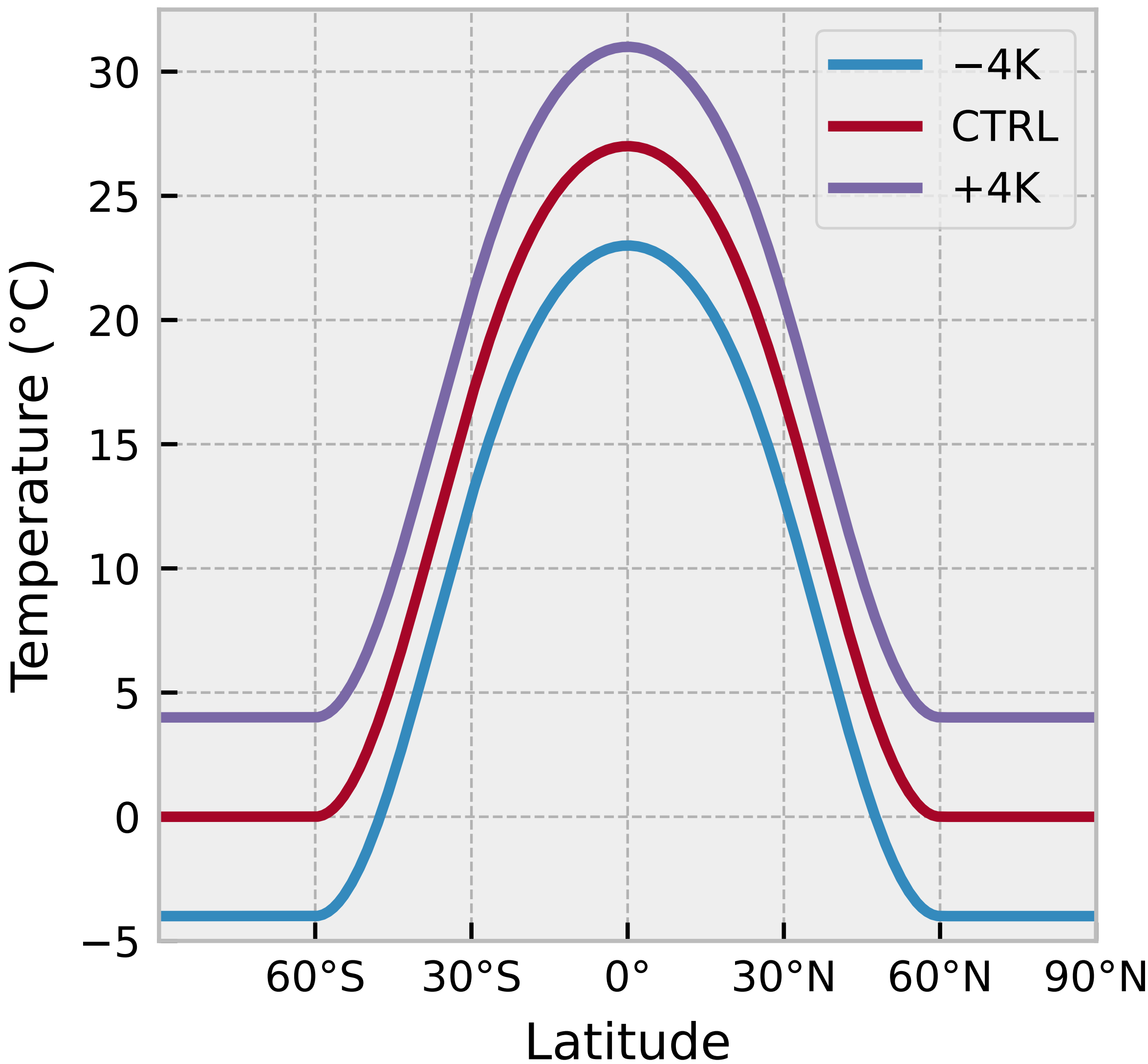

FIG. 1. ‘Qobs’ Sea Surface Temperature Profiles as a function of latitude and experimental setup, in °C.

b. Moisture Budget Analysis

Many studies have utilized column-integrated moisture or moist static energy (MSE) budgets of the MJO to quantify the role that moist processes play in MJO dynamics (Andersen and Kuang 2012; Sobel et al. 2014; Ren et al. 2021). Here we choose to examine the MJO's growth by constructing a budget for MJO-regressed column-integrated moisture anomalies (Eq. 1):

$$\frac{\partial \langle q \rangle}{\partial t} = -\left\langle u\frac{\partial q}{\partial x}\right\rangle - \left\langle v\frac{\partial q}{\partial y}\right\rangle - \left\langle \omega\frac{\partial q}{\partial p}\right\rangle + E - P, \tag{1}$$

where q is specific humidity, u and v are respectively the zonal and meridional wind velocities, ω is the vertical velocity in pressure coordinates, E represents evaporation and P represents precipitation. Angle brackets denotes a column-integral from the surface to 100 hPa: $\langle\cdot\rangle = \frac{1}{g}\int_{p_0}^{p_s}(\cdot)\,dp$.

For each term in Eq. 1, as well as the column-integrated moisture, regression coefficients were calculated at each latitude and longitude following the procedure detailed in section 2a. Each regressed budget term was then projected onto the regressed column-integrated moisture field, horizontally integrated over 15°S-15°N and all longitudes, and normalized by the horizontally-integrated column moisture variance:

$$M(\varphi) = \frac{\iint_A [\varphi \cdot \langle q\rangle]\, dA}{\iint_A \left[\langle q\rangle^2\right] dA}. \tag{2}$$

The resulting value, termed the 'contribution' for that process, gives a measure of that term's relative contribution to the growth or dissipation of the MJO's moisture anomalies. A 'positive' budget contribution to maintenance means that the net effect of a given physical process is to further moisten regions with a positive MJO moisture anomaly or further dry regions with a negative MJO moisture anomaly. In so doing, a positive contribution increases the amplitude of MJO-associated moisture anomalies, leading to MJO strengthening. Conversely, a 'negative' budget contribution means that a given process acts to reduce the amplitude of MJO-associated moisture anomalies, opposing MJO amplification.

1) Gross Moist Stability

In addition to the moisture budget, an analysis of Gross Moist Stability (GMS) was performed. Originally defined in Neelin et al. (1987) with other variations defined in subsequent papers (Raymond et al. 2009; Andersen and Kuang 2012), the GMS is a measure of the stability of the atmosphere to moist convection. GMS has been tied to the growth and propagation of the MJO in both simple linear models such as Adames and Kim (2016) and Ahmed (2021) as well as in GCM studies (Benedict et al. 2014), suggesting that it is a useful way to diagnose changes to the MJO in our simulations. The specific formulation used herein is the vertical component of normalized GMS (NGMS), which follows the definition in Inoue and Back (2015),

$$\Gamma_v = \frac{\left\langle \omega \frac{\partial h}{\partial p} \right\rangle}{\left\langle \omega \frac{\partial s}{\partial p} \right\rangle}, \tag{3}$$

where ω is the vertical pressure velocity, $s = c_p + gz$ is the Dry Static Energy (DSE) and $h = s + L_v q$ is the Moist Static Energy (MSE) defined above. The numerator in Eq. 3, which is the column-integrated vertical advection of MSE, indicates whether the column is net importing or exporting MSE; the denominator is the column-integrated vertical advection of DSE and gives a measure of the strength of the circulation within the column, which is strictly positive in ascending columns. Thus a positive NGMS, generally associated with top-heavy vertical velocity profiles that diverge high MSE air at upper-levels, corresponds to a gross moist stable column that efficiently removes MSE anomalies. Conversely, a negative NGMS corresponds to a positive feedback in which MSE anomalies in the column induce circulations that result in a net import of MSE and growth of MSE anomalies within the column.

The vertical NGMS was estimated for each experiment as the slope of the linear regression between anomalies in column-integrated vertical DSE advection and column-integrated vertical MSE advection. Both quantities were computed at each time and latitude–longitude grid point.

2) Column Process

One of the key processes relevant to the MJO's moisture budget is the 'column process' (Chikira 2014), which represents the combined effects of vertical moisture advection and precipitation that co-occur within a given column of the atmosphere. Starting from the column-integrated moisture budget (Eq. 1), the strength of the column process term can be related to the GMS. To do this, the vertical moisture advection term is first rewritten as a function of vertical MSE advection and vertical DSE advection:

$$\left\langle \omega \frac{\partial q}{\partial p} \right\rangle = \frac{1}{L_v} \left(\left\langle \omega \frac{\partial h}{\partial p} \right\rangle - \left\langle \omega \frac{\partial s}{\partial p} \right\rangle \right). \tag{4}$$

Using the definition of vertical GMS in Eq. 3, this can be expressed as:

$$\left\langle \omega \frac{\partial q}{\partial p} \right\rangle = \frac{1}{L_v} \left\langle \omega \frac{\partial s}{\partial p} \right\rangle (\Gamma_v - 1). \tag{5}$$

Then, substituting this expression into Eq. (1) yields the following:

$$\frac{\partial \langle q \rangle}{\partial t} = -\langle \upsilon \cdot \nabla q \rangle - \frac{1}{L_\upsilon} \left\langle \omega \frac{\partial s}{\partial p} \right\rangle (\Gamma_\upsilon - 1) - P + E. \tag{6}$$

This expression can be further simplified with a few key assumptions (Sobel et al. 2001):

1. Temperature tendencies and horizontal gradients are small (Weak Temperature Gradient approximation),

2. Sensible heating is small,

3. Column-integrated radiative heating is proportional to column-integrated convective heating,

4. Column-integrated convective heating is equivalent to precipitation.

Applying these assumptions to the column-integrated thermodynamic energy equation results in the following relation:

$$\left\langle \omega \frac{\partial s}{\partial p} \right\rangle = (1 + r)P, \tag{7}$$

where r is the cloud-radiative feedback parameter defined in Kim et al. (2015) as $r \equiv -OLR'/P'$. This parameter represents how vertical moisture advection can modulate local radiative cooling within a column by importing water vapor (a greenhouse gas) and producing high clouds. If the radiative heating anomaly induced by the circulation is collocated with positive buoyancy anomalies, then the circulation will strengthen and import more moisture in a process known as the Cloud-Radiative Feedback. Previous studies have established that the presence of such radiative feedbacks are key for the growth and strengthening of the MJO (Kim et al. 2015; Del Genio and Chen 2015).

Collectively, Eq. 7 represents the fact that the dominate thermodynamic balance in the tropical atmosphere is that of Weak Temperature Gradient (WTG) balance, where vertical motions in the column and their corresponding horizontal circulations work to balance diabatic heating from condensation and radiation.

Substituting this relation into Eq. 6 then produces an alternative form of the moisture budget equation that succinctly captures the contribution of the column process to MJO moistening as a function of GMS, the cloud-radiative feedback parameter, and precipitation.

$$\frac{\partial \langle q \rangle}{\partial t} = -\langle v \cdot \nabla q \rangle - \frac{P \cdot \Gamma_{\text{eff}}}{L_v} + E. \tag{8}$$

Here $\Gamma_{\text{eff}} \equiv \Gamma_v(1+r) - r$ is known as the effective GMS and accounts for both thermodynamic and radiative effects. Given that P is positive, the sign of the effective GMS determines whether the column process acts to amplify or dampen moisture anomalies.

3. Results

a. Changes to the Mean-State in Response to Warming

Given the desire to understand how warming of the mean-state projects onto changes in the MJO, it is critical to examine changes to the mean-state climatology in the different simulations.

As can be seen in Fig. 2, there are clear changes to the mean state temperature and moisture profiles of the tropical atmosphere (30°S-30°N) between the three experiments. The mean-state vertical temperature profile shows higher temperatures throughout the column in the warmer experiments, with the melting-level rising from around 700 hPa in the -4K simulation to just above 600 hPa in the CTRL and around 540 hPa in the +4K simulation. The mean-state temperature minimum, a proxy for the transition from the troposphere to the stratosphere, also rises slightly from 125 hPa in the -4K simulation to 100 hPa in both the CTRL and +4K simulations. Generally, the increase in the mean temperature is greater higher in the atmosphere (Fig. 2c), indicating a shift towards a higher static stability with higher SSTs. This is a well established result of previous climate change studies (Frierson 2006; Chou et al. 2013) and occurs because deep tropical convection acts to maintain the vertical profile of the atmosphere to be near that of a moist adiabat (Xu and Emanuel 1989). Of the three simulations, the +4K compares most favorably with ERA5 throughout the depth of the column, although the CTRL simulation begins to match more closely near the temperature minimum.

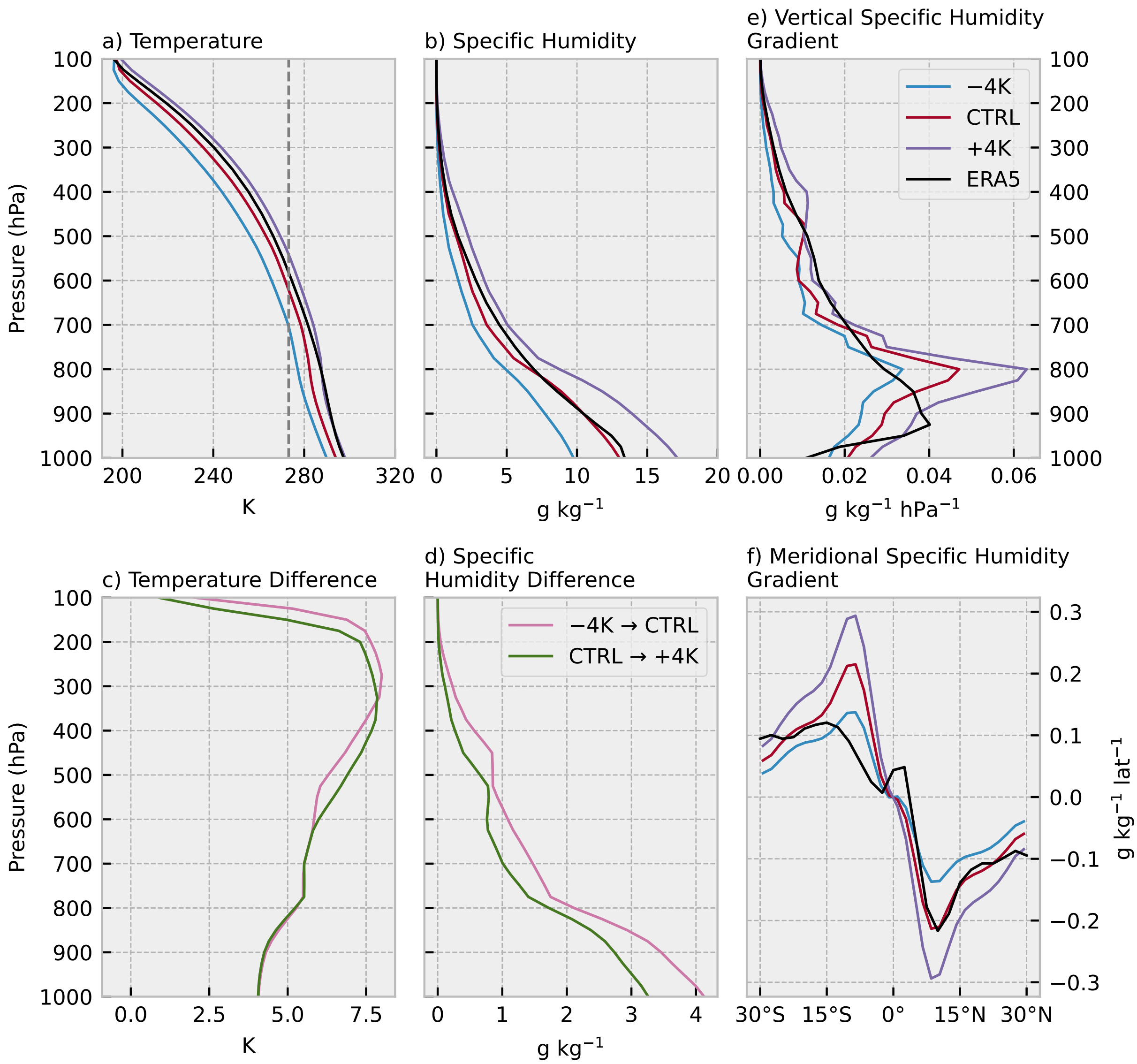

FIG. 2. Mean-state vertical profiles of a) Temperature, b) Specific humidity for each of the three experiments over the tropics (30°S-30°N), along with profiles from ERA5 Reanalysis. Panels c) and d) show the changes in mean-state temperature and specific humidity, respectively, between the -4K and CTRL simulations and between the CTRL and +4K simulations. Panels e) and f) show the vertical and meridional gradients of specific humidity for each of the three experiments as well as ERA5.

The vertical profile of the mean-state moisture and its vertical gradient also show several interesting features; in all experiments moisture peaks in the boundary layer and lower troposphere and decreases monotonically with height. The ERA5 profile largely falls in-between the CTRL and

+4K simulations, especially in the lower troposphere, but is closer to the CTRL simulation above 500 hPa. The vertical gradient of the mean-state moisture exhibits a peak at 800 hPa in all three simulations, but the magnitude of the peak is significantly larger in the +4K compared to the -4K case, showing an increase of 88.0%. By contrast, the peak in the ERA5 data occurs lower, around 900 hPa, with an amplitude more similar to that of the CTRL simulation. It is also worth noting that the three simulations show generally higher column relative humidity than ERA5, with averages between 30°S-30°N of 64%, 60%, and 57% for the -4K, CTRL, and +4K experiments respectively, compared to 50% for ERA from November-April. This discrepancy likely results from the absence of land in our simulations, and is mitigated somewhat when comparing the simulations to the Warm Pool, which has an average column relative humidity between 10°S-10°N and 90°E-150°E of 70%.

The meridional moisture gradient also increases with warming, as seen in Fig. 2f, with 56% and 38% increases in the maximum value from -4K to CTRL and CTRL to 4K, respectively. The latitude at which the highest meridional moisture gradient occurs remains constant however, at 8.5° poleward of the equator in both hemispheres.

Quantifying the change in column moisture as a function of warming gives a mean increase in column water vapor over the tropics of 9.64%/K, slightly higher than predictions based on Clausius-Clapeyron scaling. Additionally, the increase in tropical mean precipitation of 3.49%/K is high relative to the estimate of Held and Soden (2006). Despite this, our results suggest that to first-order, the mean-state atmospheres in our simulations represent the real tropical atmosphere reasonably well.

b. Changes to the Madden-Julian Oscillation in Response to Warming

Shown in Fig. 3 are normalized, equatorially-symmetric power spectra of precipitation (Wheeler and Kiladis 1999) corresponding to the three experiments. The CTRL experiment (Fig. 3b) shows a power spectrum that is qualitatively consistent with observations: there are slow eastward and westward propagating signals corresponding to the MJO and to equatorial Rossby waves, as well as an eastward-propagating signal between 2-10 days corresponding to equatorial Kelvin waves. However, in the CTRL spectrum the strongest signal occurs in the westward Rossby-wave domain as opposed to the observed peak in the eastward MJO-domain.

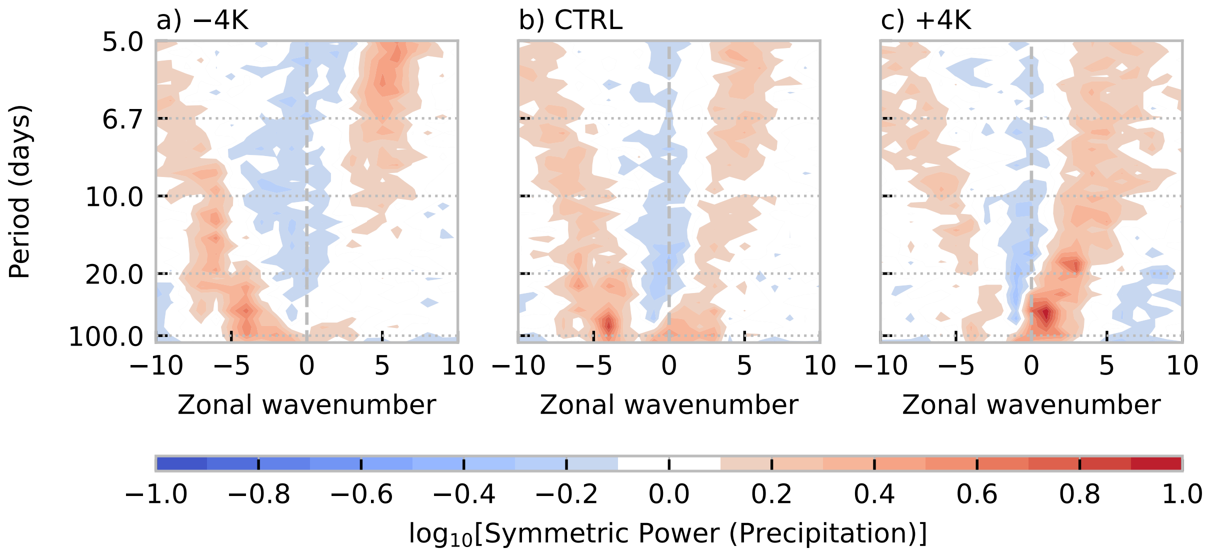

FIG. 3. Logarithm of symmetric spectral power for the (a) -4K experiment, (b) CTRL experiment, and (c) +4K experiments. In all experiments, the data was averaged between 30°S-30°N

The east-west power ratio, calculated as the ratio of the summed eastward power between 20-100 days and wavenumbers 1-6 and the summed westward power over the same region for the CTRL case is 0.748, indicating that more power is contained within the westward-propagating wave signal. In the -4K simulation, the east-west asymmetry becomes even more extreme, with an east-west power ratio of 0.606 resulting from the near-total absence of signal in the eastward-propagating MJO-band as well as the enhanced power of the westward-propagating Rossby band. The east-west ratio of the +4K simulation is 1.81, confirming a significant strengthening of eastward-propagating signals with warmer SSTs. In comparison, the east-west power ratio calculated from TRMM precipitation data between 2001 and 2014 over the tropical oceans is 1.19.

Taken together, Fig. 3 shows a clear transition with mean surface warming from a regime in which westward-propagating signals are dominant to a regime in which eastward-propagating signals are dominant. These results are consistent with several other studies that have examined the effects of warmer mean states on the MJO in aqua-planet simulations, such as Arnold et al. (2013) and Carlson and Caballero (2016). In contrast, Rushley et al. (2019) examined several CMIP5 models with simulations run under the representative concentration pathway (RCP) 8.5 scenario, in which greenhouse gas emissions are specified, and found that both eastward- and westward-propagating

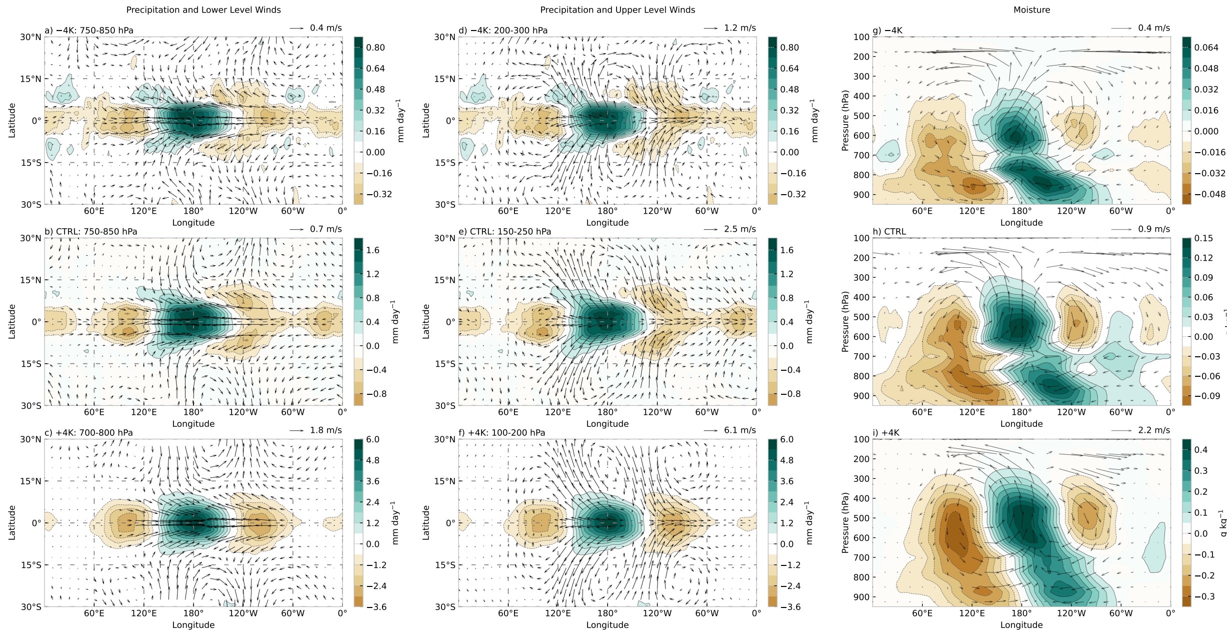

FIG. 4. Horizontal structures of MJO-regressed precipitation and horizontal winds at lower levels (Left) and upper levels (Center). (Right) Longitude-height structures of MJO-regressed moisture and zonal and vertical winds for each of the three mean-state experiments, averaged over the near-equatorial region specified. Note that vertical velocity values are scaled by a factor of 360 for visualization purposes and that the colorbar limits increase from top (-4 K) to bottom (+4 K).

wave signals increase with warming, attributing the changes in MJO variability to changes in the tropical precipitation variability. Questions remain as to both where these differences arise from, be it the absence of land in these simulations, the different forcings used (i.e. greenhouse gas emissions vs. specified SSTs), or some other factor, as well as to the implications of these differences for the observed MJO in future climates.

1) Horizontal and Vertical Structure of the MJO

Figures 4a-c and 4d-f show the horizontal structure of the MJO-associated precipitation as well as the zonal and meridional wind anomalies averaged over 100 hPa thick layers of the lower and upper troposphere, respectively. The layers were chosen by first constructing the Empirical Orthogonal Functions (EOFs) of intraseasonally-filtered vertical velocity for each of the three experiments separately, which identified a single baroclinic mode as the dominant structure explaining, on average, 86% of the variance across each of the three experiments. Then, the continuity equation was used to construct the corresponding mode structure of the horizontal winds, from which two peaks were identified for each experiment: one in the lower-troposphere and one in the upper-troposphere. The precipitation anomalies are the same between the two figures. Figs. 4g-i show the longitude-height structures of the MJO-associated moisture field as well as rescaled zonal and vertical winds averaged between 15°S-15°N. Note that since the MJO propagates eastward in time, locations east of the reference longitude can be understood as preceding the precipitation peak, whereas locations to the west of the reference longitude equivalently trail the precipitation peak.

In some ways the CTRL experiment compares favorably with the observed MJO; there is a positive precipitation anomaly centered on the equator at the reference longitude which co-occurs with low-level zonal convergence. Both preceding and following the peak precipitation are regions of negative anomalous precipitation corresponding to the descending branch of the MJO. Unlike the observed MJO, however, the CTRL experiment does not exhibit strong off-equatorial gyres at either lower or upper levels. Fig 4b shows a strong cyclonic flow extending from approximately 10° poleward of the equator out beyond 30°, but it occurs ahead of the precipitation peak as opposed to trailing it. The vertical structure of the MJO in the CTRL experiment (Fig. 4h) shows strong vertical motion collocated with the equatorial precipitation maximum at 180°, as well as the 'shallow-to-deep' transition seen in the observed MJO (Mapes et al. 2006), wherein low-level moistening precedes the deep convective phase of the MJO while large-scale subsidence drys the atmosphere in its wake.

Qualitatively, the +4K experiment (Fig. 4c) exhibits a structure that is quite similar to that of the CTRL experiment, with a precipitation peak occurring on the equator centered around 180° longitude and flanking regions of negative precipitation anomalies to the east and west. The structure of the leading negative precipitation anomaly differs between the two, with the CTRL experiment showing a bimodal peak slightly poleward of the equator, whereas the +4K experiment exhibits a single, on-equatorial peak. Furthermore, the amplitude of the peak precipitation anomaly is significantly higher in the +4K experiment; the peak precipitation in the CTRL experiment is 1.9 mm day^{-1}, as compared to 6.1 mm day^{-1} in the warmer climate, a three-fold increase. The +4K experiment also has generally stronger horizontal winds, except for the region between 60°W and 0°, where the CTRL experiment shows strong easterlies that do not appear in the +4K experiment. The upper-level wind anomalies (Fig. 4e,f) are also qualitatively similar, with the exception of

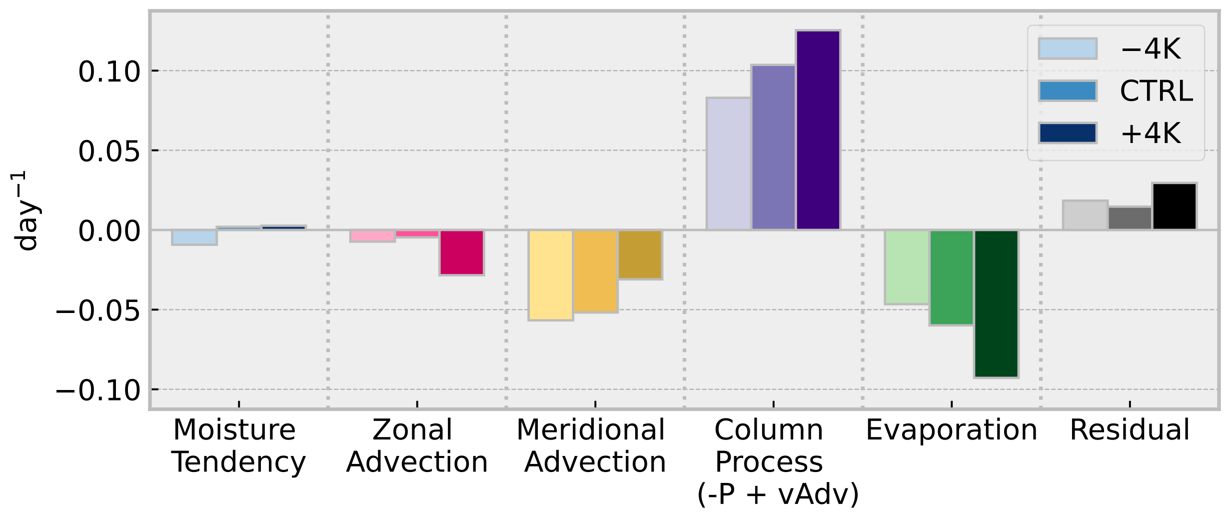

FIG. 5. Relative contribution of each moisture budget term to the maintenance of the MJO's moisture anomaly. The 'column process' term is the sum of precipitation and vertical moisture advection.

a much stronger cyclonic flow centered around 90°W in the +4K experiment that appears only weakly in the CTRL experiment. Note also that the level of maximum divergence rises slightly with warming, from 200 hPa to 150 hPa, but remains at nearly a constant temperature (not shown).

Examining the vertical structure of the +4K experiment shows that the shallow-to-deep transition still occurs, with a three-fold increase in the magnitude of the peak moisture anomaly when compared to the CTRL experiment. There is also a transition in the structure of the positive moisture anomaly, which has a single upper-level peak in the +4K experiment, as compared to relatively equal upper and lower-level peaks in the CTRL experiment. As with the upper-level winds, the moisture anomalies extend vertically to a higher level with warming.

Compared to the MJO in both the CTRL and +4K structures, the MJO in the -4K experiment is relatively weak, with a maximum precipitation anomaly of only 0.8 mm day^{-1}, while the negative precipitation anomalies extend nearly continuously on either side of the precipitation maximum. There is still strong low-level convergence that is collocated with the precipitation peak, but the off-equatorial flow has a less longitudinally consistent structure when compared with the CTRL and +4K experiments. At upper levels there is a region of broad anti-cyclonic outflow as with the warmer two experiments, but it is both less meridionally tilted and less latitudinally extensive. The corresponding vertical structure shows the familiar deep inflow pattern with low-level convergence and upper-level divergence, as well as two relatively equal magnitude moisture peaks, as in the CTRL simulation. Unsurprisingly, the magnitude of the maximum moisture anomaly is weaker than that of the CTRL, peaking at around 0.07 g kg^{-1}, and occurs lower in the troposphere than the corresponding upper-level peak in the CTRL and +4K simulations.

Collectively, Fig. 4 shows that the main effect of warming is to considerably strengthen the MJO-regressed precipitation, wind, and moisture anomalies. There are slight structural changes as well, with warming leading to more vertically-extensive anomalies, while the dominant zonal scale of the MJO does not significantly change with warming. Furthermore, the changes seen are consistent with both the strong increase in MJO-domain spectral power seen in Fig. 3, and other studies of changes to the MJO with warming (Arnold et al. 2013; Adames et al. 2017; Rushley et al. 2019).

2) Moisture Budget Analysis

The results of the moisture budget analysis described in Section 2 are presented in Fig. 5. In all three experiments, growth results almost entirely from the column process term, while horizontal advection and evaporation act to damp the MJO. Given our focus on understanding the causes of MJO strengthening with warming, we limit our discussion to the two processes that monotonically increase with warming and as such result in higher MJO-associated moisture variability: the column process and meridional advection.

(i) Column Process Column integrated vertical advection, which is equivalent to net moisture convergence into the column, positively contributes to MJO maintenance by moistening regions that are already moist. In particular, strong vertical winds and low-level convergence are collocated with positive low-level moisture anomalies near the deep convective center of the MJO. The deep convective flow imports anomalously moist air into the column which is often advected into the upper atmosphere. Above the lifting condensation level, condensation of the advected moisture and the fallout of precipitation to the surface will occur, removing moisture from the column. The column process, introduced previously, conveniently combines these two effects of vertical motion on column moisture into a single term.

If the same vertical wind anomaly converges more moisture into an anomalously moist column than is lost to precipitation, the column process acts to amplify the moist anomaly. This is the case

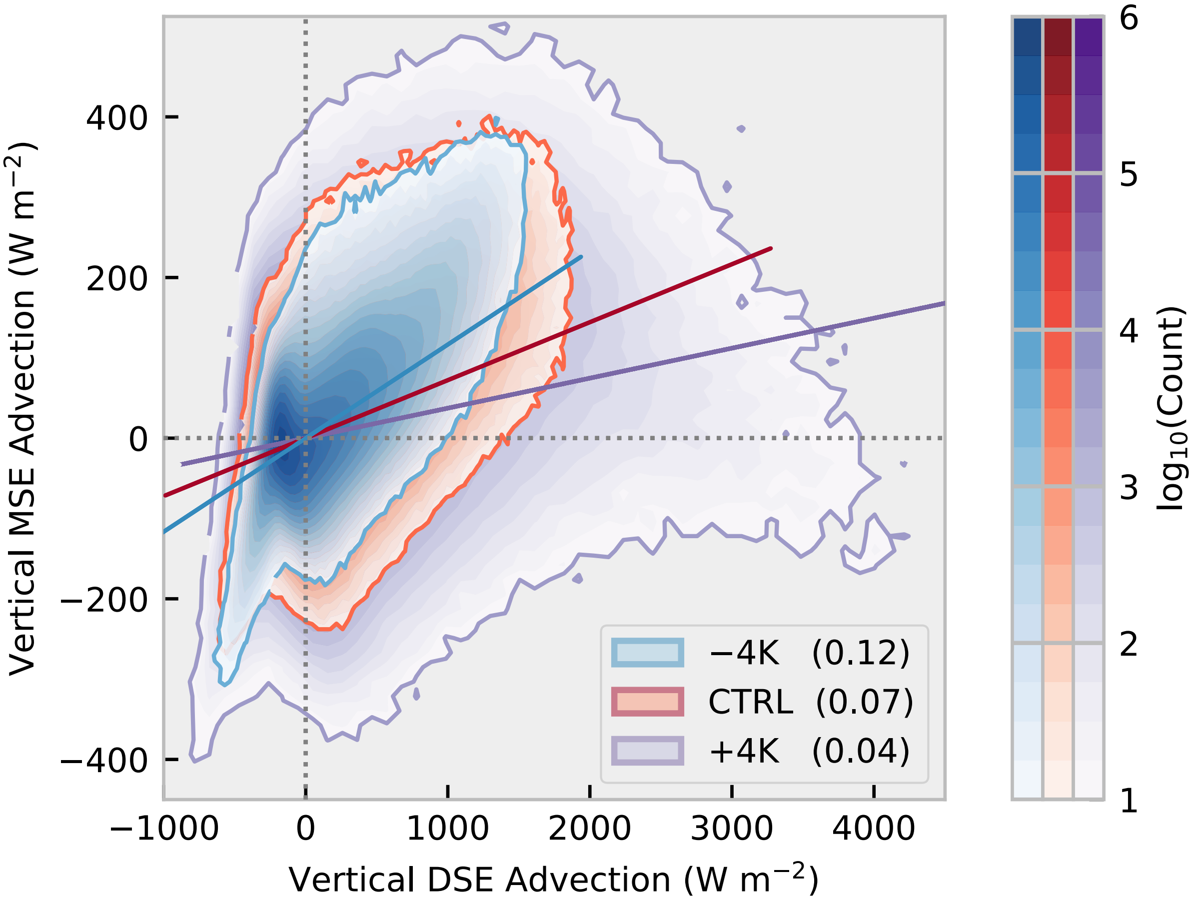

FIG. 6. Vertical component of normalized Gross Moist Stability, computed for each time and longitude-latitude grid location between 15°S-15°N.

for all three experiments, where the column process contributes positively to MJO maintenance, and in fact it becomes a larger source of column moisture with warming. Considered separately, the drying associated with precipitation and the moistening associated with vertical advection both weaken slightly with warming (not shown); the column process' increasingly positive contribution results from the drying weakening more than the moistening. This change in the column process can be explained largely through changes in the GMS, shown in Fig. 6.

Gross Moist Stability In all experiments the estimated vertical NGMS is positive, indicating a gross moist stable environment. However, the value of the NGMS decreases slightly with warming such that the environment becomes less stable to MSE perturbations. In the mean-state, smaller

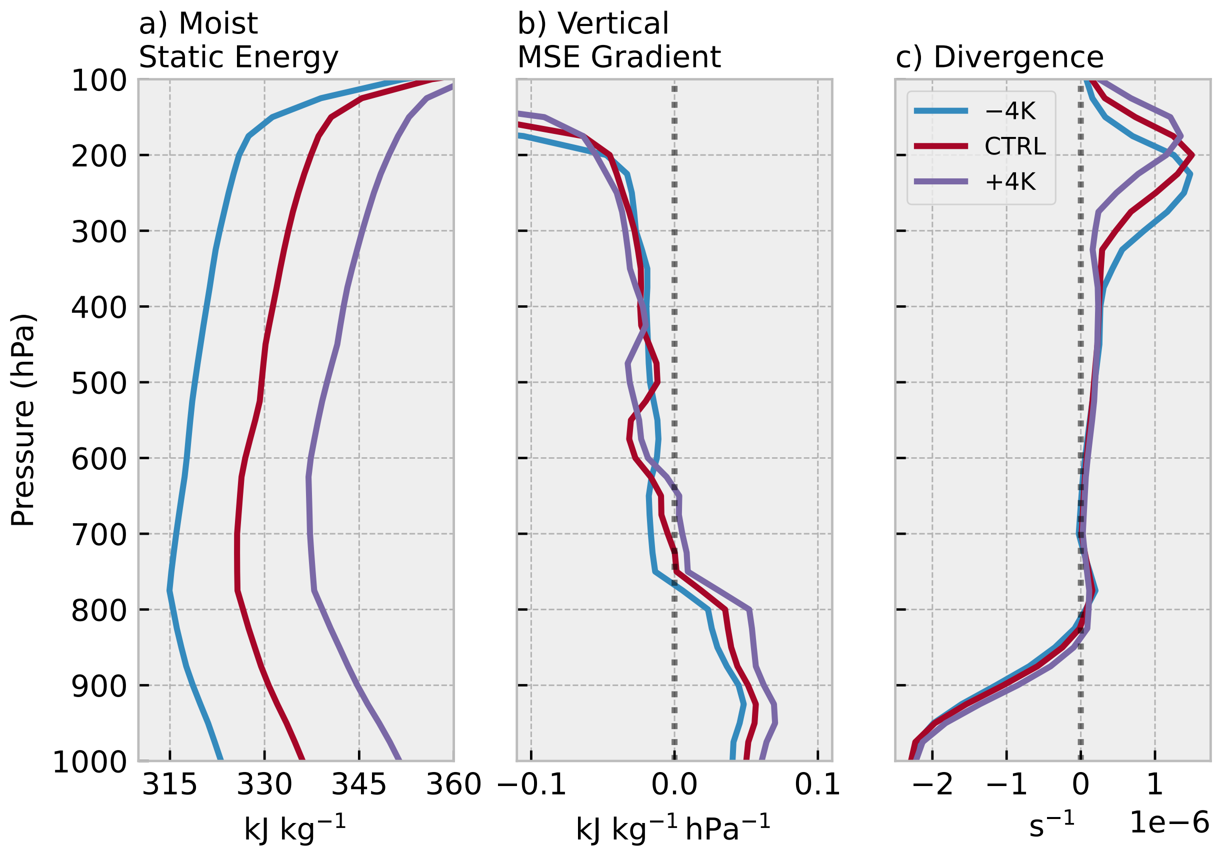

FIG. 7. Mean-state vertical profiles of (a) Moist Static Energy, (b) the vertical gradient of MSE, and (c) the divergence for each of the three experiments.

NGMS arises from a reduction in the net MSE export associated with weaker column-integrated vertical MSE advection. Fig. 7 shows the mean-state vertical profiles of MSE, the vertical gradient of MSE, and the divergence for each of the three experiments.

The mean state vertical MSE profile shows similar structure in all three experiments, with a local maximum near the surface resulting from high moisture and a maximum in the upper-troposphere associated with high geopotential heights. A minimum occurs in all three experiments in the mid-low troposphere associated with the exponential decay of moisture with height and the relatively low geopotential heights at that level. The main difference between the three experiments is in the vertical mean, with substantially higher values throughout the troposphere with warming, associated with both a deeper and moister troposphere.

However, there is also an important increase in the low-level vertical MSE gradient with warming, as seen in Fig. 7b. Taking a vertical mean over the levels with mean-state horizontal convergence shows that the vertical MSE gradient increases from 0.38 $\mathrm{J\,kg^{-1}\,Pa^{-1}}$ in the -4K experiment to 0.49 and 0.63 $\mathrm{J\,kg^{-1}\,Pa^{-1}}$ in the CTRL and +4K experiments, respectively. Thus, for similar low-level convergence, the +4K experiment imports nearly 27% more MSE into the column compared with the CTRL experiment. At upper-levels, where there is horizontal divergence and net MSE export, the vertical MSE gradient is more similar across the three experiments, with values of -0.17, -0.15 and -0.14 $\mathrm{J\,kg^{-1}\,Pa^{-1}}$ in the -4K, CTRL and +4K experiments, respectively. Taken together, the increase in the low-level vertical MSE gradient with warming results in a stronger import of MSE into the column in the +4K experiment that is not sufficiently compensated by upper-level export, leading to stronger convection and enhanced background variability.

Ultimately, the increase in the lower-level vertical MSE gradient seen in Fig. 7 is a function of the sharp increase in the lower-level specific humidity gradient, seen previously in Fig. 2d, resulting from the Clausius-Clapeyron relationship.

Cloud-Radiative Feedbacks To quantify the role that cloud-radiative feedbacks play in the growth of the MJO, the cloud-radiative feedback parameter was estimated from the slope of the OLR-precipitation relationship. The resulting estimates have values of 0.16, 0.14, and 0.10 for the -4K, CTRL, and +4K simulations, respectively (Fig. 8), which are well-aligned with estimates of the real atmosphere such as from Peters and Bretherton (2005) and Adames and Kim (2016), suggesting that the simulations have a realistic OLR-precipitation relationship.

Combining the intraseasonal r estimates with the estimated values of GMS produces values for the effective GMS of -0.015 for the -4K experiment, -0.034 for the CTRL experiment, and -0.038 for the +4K experiment. Plotting the effective GMS (Fig. 9) as a function of its two constituent parameters reveals the relative contributions of each component to the quantity.

Effective GMS, which is inversely related to MJO strength, generally decreases with decreased NGMS as discussed previously. However, it also increases with a decrease in r, since a reduction in anomalous radiative heating associated with a weaker cloud-radiative feedback will tend to weaken the MJO, meaning that reductions in both GMS_v and r with warming offset one another. Transitioning from -4K to CTRL, the decrease in GMS_v is larger than the decrease in r, leading

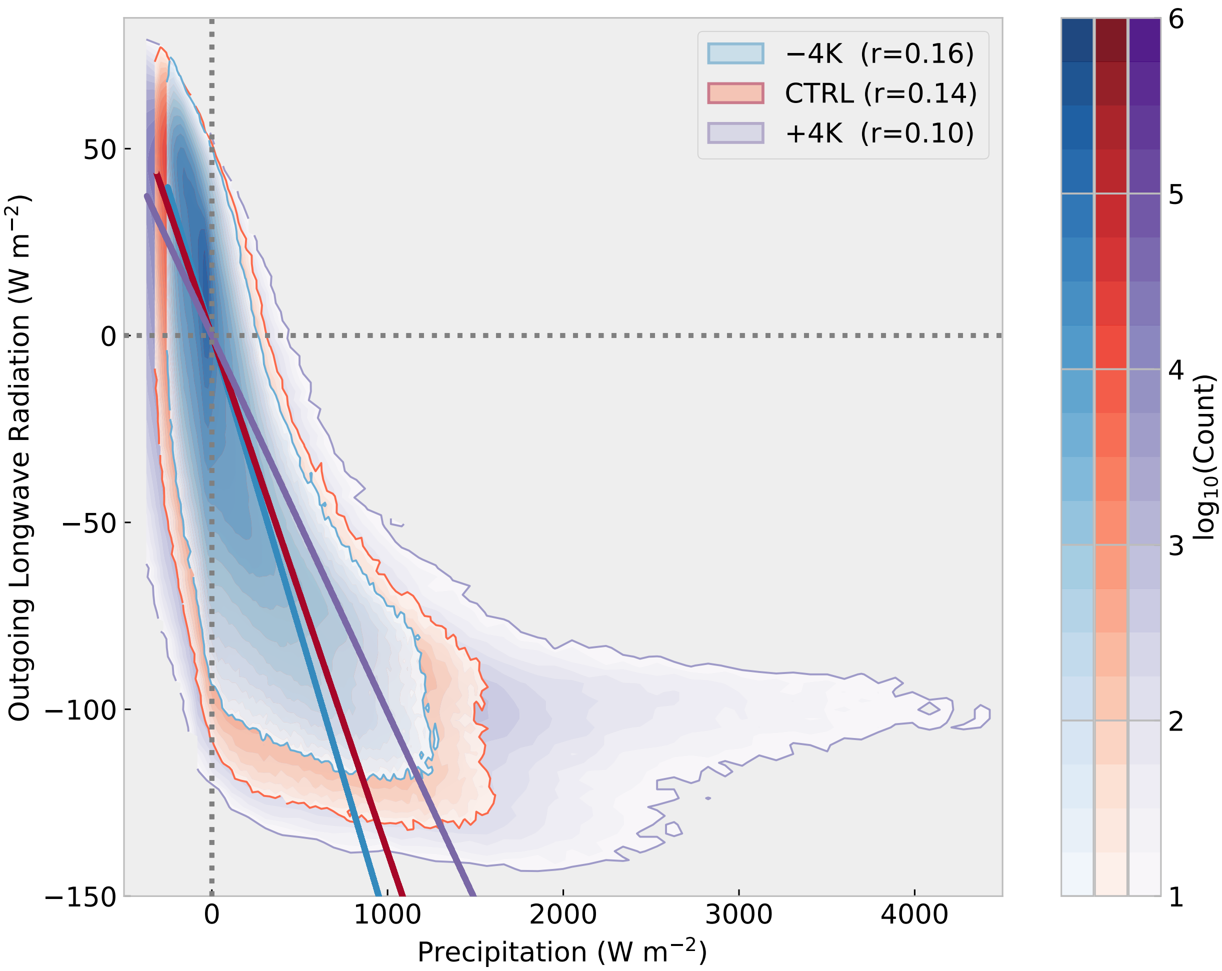

FIG. 8. Anomalous precipitation vs. OLR computed for each time and longitude-latitude grid location between 15°S-15°N. The cloud-radiative feedback parameter is estimated as the slope of the best-fit line for each experiment.

to a relatively large reduction in the effective GMS (Fig. 9). From the CTRL simulation to the +4K, however, the two terms are of approximately equal magnitude, resulting in a much smaller reduction in effective GMS. This can be explained by examining the change in r seen in Fig. 8; in all three experiments, the largest precipitation anomaly increases considerably with warming from around 1250 W m^{-2} to well over 2500 W m^{-2}. In contrast, the minimum OLR value changes considerably less with warming, ranging from -125 W m^{-2} in the -4K experiment to around -150 W m^{-2} in the +4K experiment.

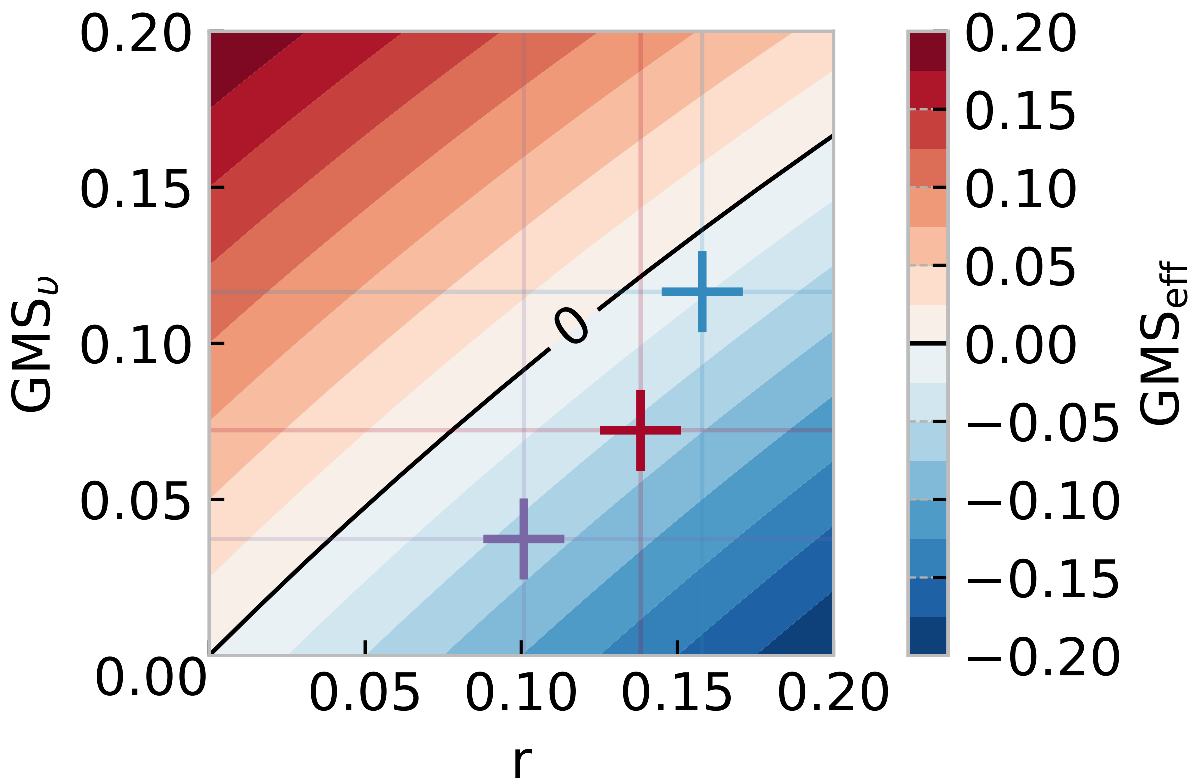

FIG. 9. Effective Gross Moist Stability (colors) as a function of cloud-radiative feedback parameter r and normalized vertical GMS. Estimates of r and GMS$_v$ for each of the three experiments are shown as 'plus' signs on the plot.

Physically, these precipitation and outgoing longwave radiation values correspond to the most convectively active regions in the atmosphere, with deep convective cores that produce significant rainfall and extensive high anvil clouds that strongly modify longwave radiative cooling. Figures 10a-c show cloud fraction binned by cloud ice water path percentile (which acts as a measure of deep convective strength) and temperature (which is analogous to height) for the -4K, CTRL, and +4K experiments respectively. Figure 10d shows the cloud ice water path for each percentile, showing a sharp increase in cloud ice water path around the 97th percentile, with values between 20-30 g m^{-2}. Figs. 10a-c show that cloud fraction is at or above 90% throughout much of the upper troposphere for the same percentiles, meaning that convectively active regions have essentially ubiquitous cloud cover. Taken together, the high cloud fraction and high cloud ice water path (and as such high longwave optical depth) indicate that such regions are emitting approximately as blackbodies. Furthermore, Figs. 10e and f show that while precipitation in the high cloud ice water percentile regions increases significantly with warming, outgoing longwave radiation converges beyond the 97th percentile, in line with what was shown in Fig. 8.

As the most convectively active and heavily precipitating columns of the simulation are nearly blackbodies, their longwave emission is solely a function of cloud top temperature; given this we hypothesize that OLR in these simulations is predominately controlled by the Fixed Anvil Hypothesis (FAT) of Hartmann and Larson (2002), which proposes that the emission temperature of tropical anvil clouds should remain nearly invariant with surface warming. Figure 11 shows the domain-mean cloud ice water content as a function of temperature for each of the three experiments, which acts as a proxy for the height of tropical anvil clouds. Following the FAT hypothesis, tropical anvil clouds preferentially detrain at the level where clear sky radiative cooling by water vapor becomes small, resulting in vertical mass flux divergence that must be balanced by convective anvil outflow. Given that water vapor emission is only a function of temperature, FAT predicts that the upper-level temperature at which this occurs will be independent of surface warming. Fig. 11 reveals that the FAT mechanism holds for each of the three experiments, which all peak in cloud ice water content at 220 K. Hence, the OLR in these convectively active regions remains essentially constant with warming despite significant increases in precipitation, resulting in a weaker cloud-radiative feedback that opposes MJO strengthening.

(ii) Meridional Advection As mentioned previously the meridional advection term is negative in all three experiments, and as such acts to dampen the MJO. However, it also weakens in magnitude monotonically with warming, resulting in stronger MJO-associated moisture anomalies in warmer climates.

Following Andersen and Kuang (2012), insight can be gained into the meridional advection term by decomposing both of its constituent fields - the meridional wind and the meridional moisture gradient - across multiple timescales. The three timescales of relevance in this analysis are:

1. A mean-state term obtained by taking the time-mean of the field,
2. An MJO component obtained by filtering the field for 20-100 day propagating signals,
3. A high-frequency residual component, obtained by subtracting the mean-state and MJO-filtered components from the total field.

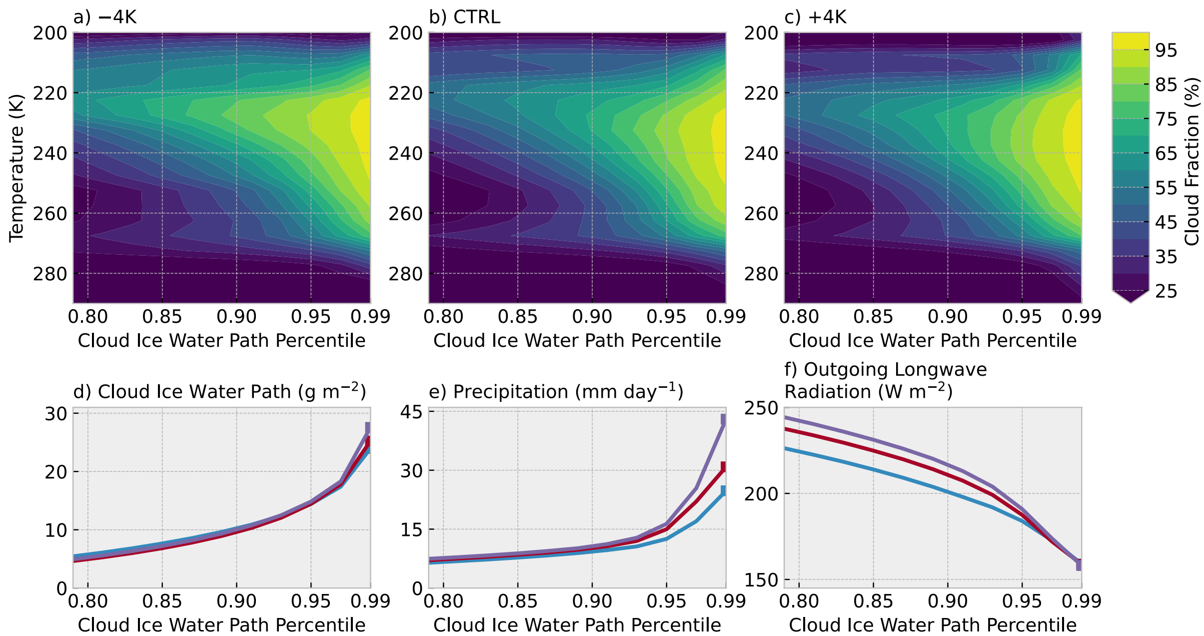

FIG. 10. Cloud Fraction binned by OLR and Temperature for each of the three experiments.

Cross-multiplying the resulting terms for each field then yields nine components that quantify the contribution of processes within and across various timescales to the total meridional advection term, the results of which are shown in Fig. 12. Note that three terms with small amplitude contributions are not shown here, the three terms being the advection of mean moisture by the mean winds, and the two terms representing advection of residual-scale moisture by the mean wind and the advection of mean moisture by the residual winds.

The largest positive term is the advection of mean-state moisture by the MJO-associated winds, $-\left\langle \upsilon_{\mathrm{MJO}} \cdot \partial_y \bar{q} \right\rangle$, whose horizontal structures can be seen in Figure 13. Since the mean meridional moisture profile has a single peak on the equator and decreases towards the poles, equatorial winds will tend to dry the MJO whereas poleward winds will result in moistening. The MJO-associated flow, as shown previously in Figs. 4a-c is broadly poleward to the east of the precipitation maximum and equatorward to the west, resulting in the moistening and drying patterns seen in Fig. 13. For a given wind anomaly, the strength of the moistening or drying will be augmented by the strength of the meridional moisture gradient. Given the Clausius-Clapeyron relation, it is expected that regions with high moisture content will experience relatively larger increases in specific humidity with warming than drier regions, resulting in a stronger equator-to-pole moisture gradient. This holds true in the simulations, which show a significantly stronger moisture gradient meridionally

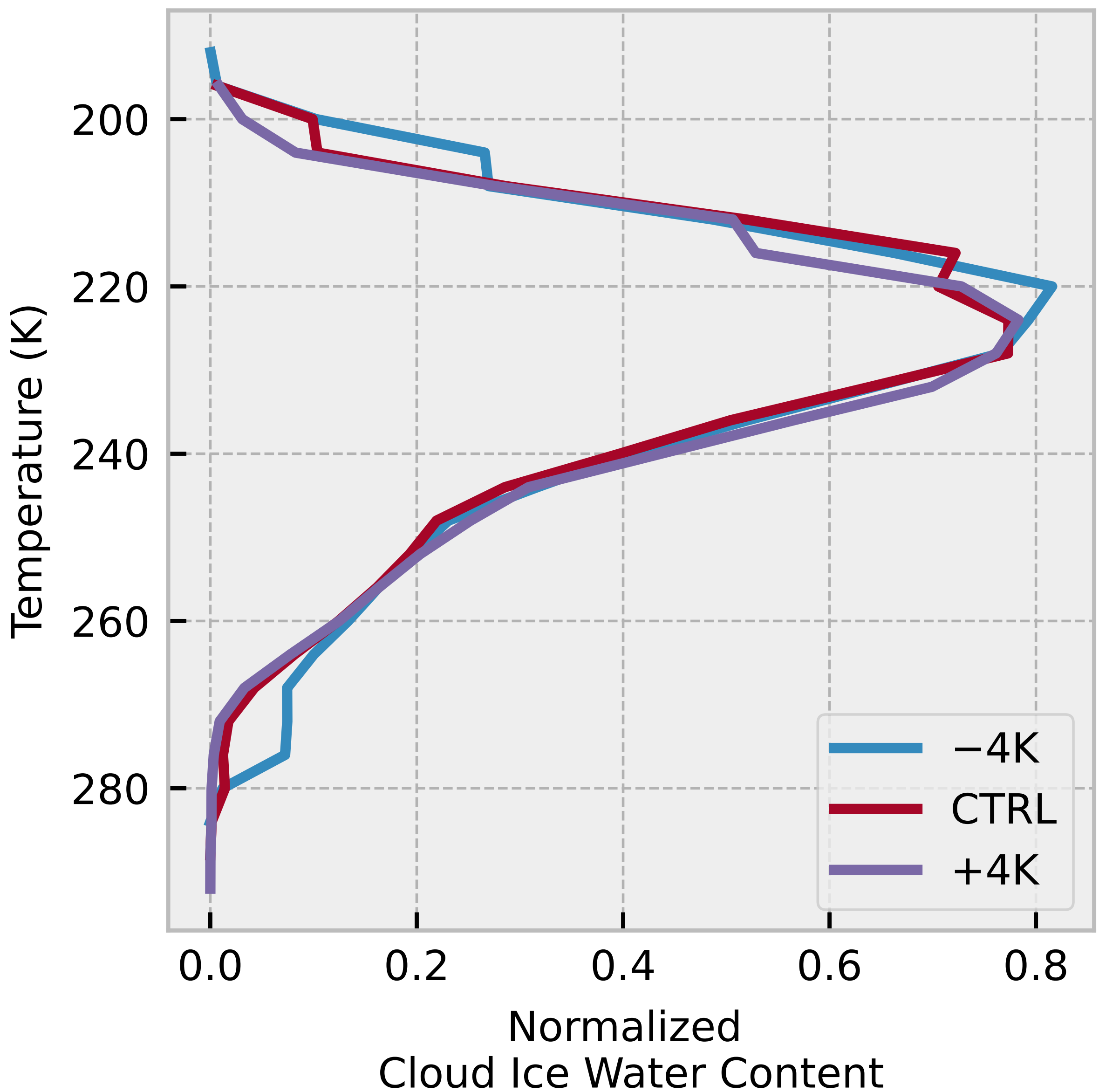

Fig. 11. Cloud Ice Water Content binned by temperature for each experiment, normalized.

(Fig. 2f), and explains in large part the increased positive moistening associated with the mean moisture gradient.

The other relevant component of the meridional advection term is the advection of MJO-associated moisture by the mean-meridional wind, $-\left\langle \bar{v} \cdot \partial_y q_{\mathrm{MJO}} \right\rangle$, which transitions from a weakly damping term in the -4K experiment to a weakly amplifying term in the +4K experiment (Fig. 14). The mean meridional wind corresponds essentially to the Hadley circulation, with equatorward

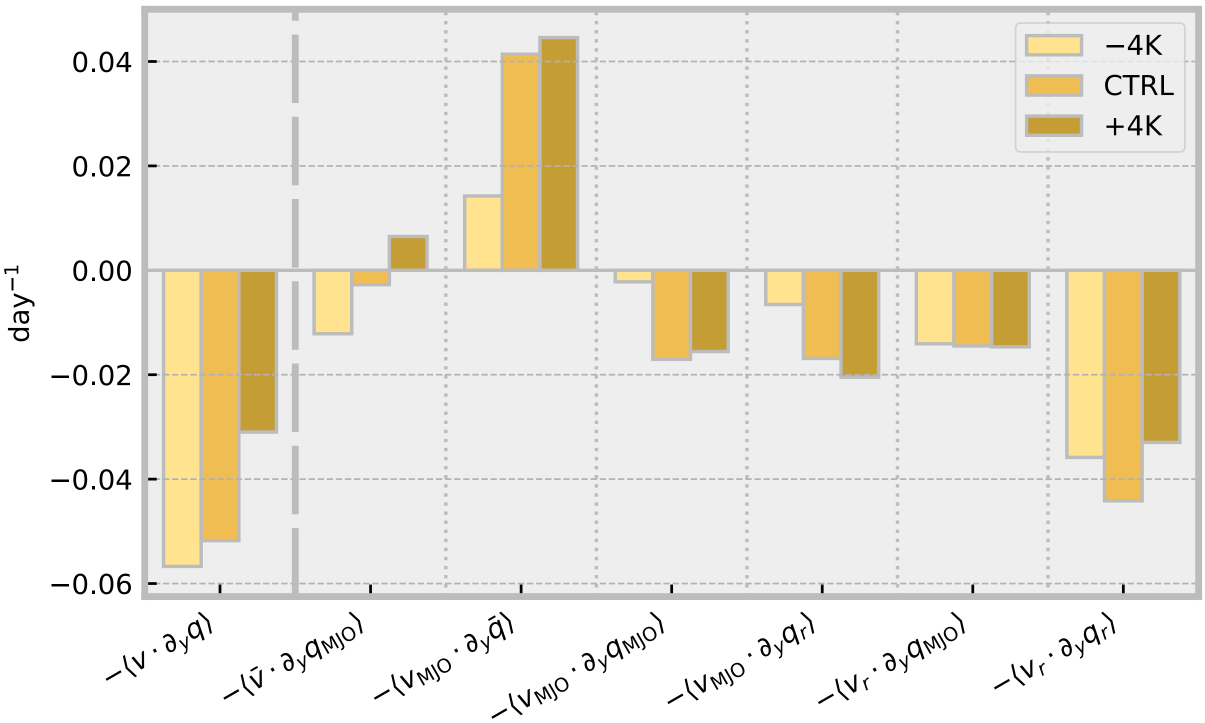

FIG. 12. Meridional moisture advection budget contribution separated into six components as a function of timescale.

flow at low-levels and poleward flow aloft. The strongest contribution to growth occurs in the +4K experiment, where moistening centered around 5°N/S is in-phase with the MJO's positive moisture anomaly. This moistening results from the horizontal pattern of the low-level (900-1000 hPa) MJO-regressed moisture, which has a local minimum around 10°N/S (not shown) that induces a small equator-to-pole moisture gradient. This, when coupled with the mean low-level equatorward flow of the Hadley cell, produces positive moisture advection. In the -4K and CTRL experiments the same moistening occurs but is phase shifted slightly westward and is thus less in phase with the MJO's positive moisture anomaly, resulting in a weaker (or net negative in the -4K case) contribution to MJO growth. The precise mechanism controlling the zonal phase relation between the meridional winds and the MJO's moisture anomaly, however, remains unclear. There is also a contribution to moistening from upper-level processes; the vertical tilting of the MJO results in a positive upper-level moisture anomaly centered at 180° with a peak on the equator, creating

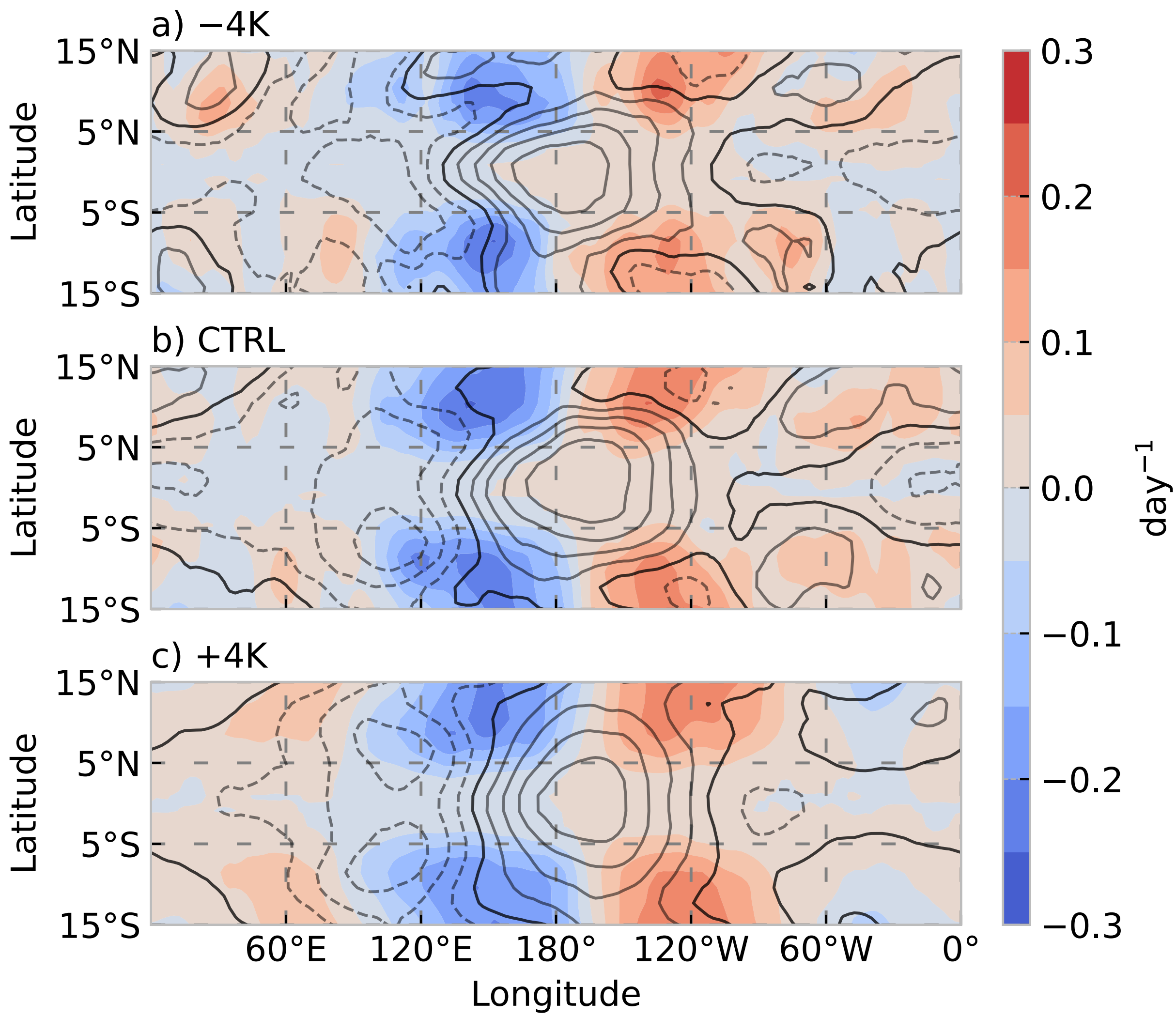

Fig. 13. Horizontal structures of moistening and drying associated with meridional advection of mean moisture by the MJO-scale winds (colors) and MJO-regressed column moisture (contours).

an equator-to-pole moisture gradient. At upper-levels the mean meridional winds are strongly poleward and this results in positive advection of MJO moisture which amplifies the MJO.

4. Summary & Conclusions

In this study, we've utilized novel aqua-planet simulations performed in a CMIP6 generation model to investigate the mechanisms leading to growth of the MJO in future warming scenarios. In many ways, the changes in the behavior of the simulated MJO with warming seen in this study are

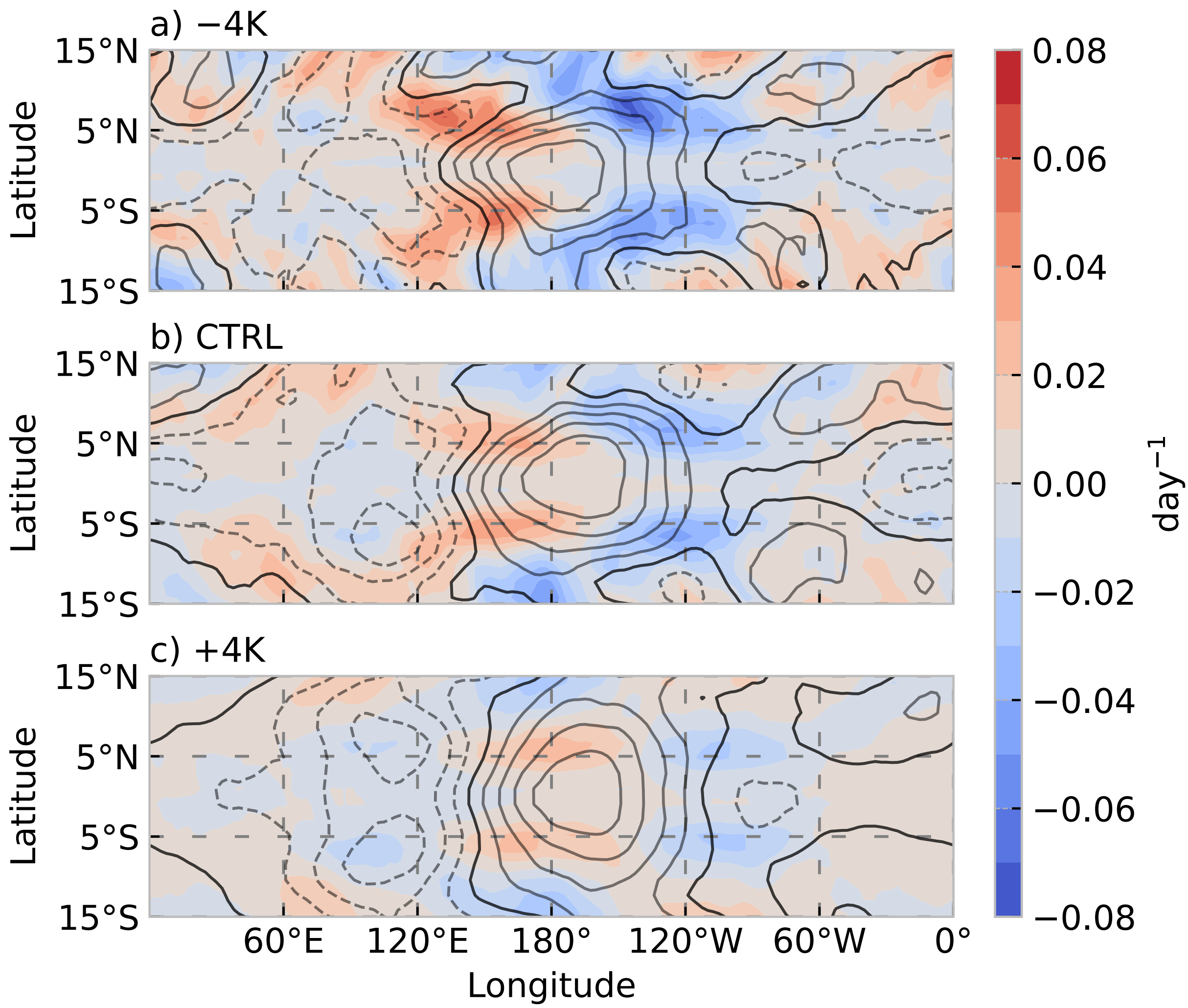

FIG. 14. Horizontal structures of moistening and drying associated with meridional advection of MJO-scale moisture by the mean winds (colors) and MJO-regressed column moisture (contours).

consistent with previous results. Examining the space-time power spectrum of the tropics shows that MJO-band power increases significantly with SST warming, indicative of a stronger MJO and higher MJO-associated variance. Unlike several previous studies, however, the east-west power ratio changes with warming, increasing non-linearly from the -4K to CTRL and from the CTRL to +4K experiments. While the strengthening of the MJO and thus the resulting increase in MJO-band power was examined in this work, understanding changes to Rossby waves with warming is left for future work.

A regression analysis reveals the structure of the MJO in each of the experiments, which exhibit qualitatively similar MJO-associated precipitation fields across the three mean-states. Similar to the observed phenomenon, the MJO-associated precipitation features a strong, central on-equatorial peak along with weaker negative precipitation anomalies preceding and following it. With warming, the magnitudes of the MJO-regressed anomalies increase considerably, in line with both the increase in MJO-band spectral power and the results of previous studies. Notably, the MJO-associated precipitation maximum increases even relative to the mean-state precipitation, unlike results shown in Pritchard and Yang (2016), in which the ratio of MJO-associated precipitation to mean-state precipitation was relatively insensitive to the underlying SST.

By utilizing a moisture budget approach, the relative importance of different processes to the growth of the MJO's moisture anomalies were quantified. In this study, MJO strengthening with warming can be attributed both to changes in the column process and to changes in the meridional advection term. Increased moistening associated with the column process result from a reduction in the vertical GMS with warming, signaling a transition of the mean-state atmosphere to one more favorable to the development of deep convection. Fundamentally, this occurs because the low-level mean-state vertical moisture gradient strengthens due to Clausius-Clapeyron in the presence of a fixed SST boundary condition. While a strengthening of the low-level moisture gradient is expected under real conditions and has been documented in coupled atmosphere-ocean models, the degree of strengthening may be overrepresented in this study.

These results support some previous studies which have looked at the relationship between GMS and the MJO, such as Benedict et al. (2014), which found that a lower normalized time-mean GMS corresponds to better simulation of the MJO in several GCMs. It is also worth mentioning, however, that previous studies examining changes in GMS with warming have instead found an increase in tropical GMS in a warmer climate; Chou et al. (2013), for example predicts an increase in tropical GMS in some CMIP3 and CMIP5 models under the RCP8.5 scenario. As such, further research into the relationship between future warming and GMS is warranted, particularly in the latest generation of models.

Additionally, we find that increases in MJO amplitude associated with vertical advection of moisture are buffered by a weakening of the mean-state cloud-radiative feedback which projects onto the MJO. While many studies have highlighted the key role that radiative processes play in amplifying the MJO (Andersen and Kuang 2012; Sobel et al. 2014; Ren et al. 2021), the reduction in the longwave cloud-radiative feedback parameter and its mechanism have not been discussed much in the literature. Given that the most convectively active columns in all three experiments tend to have near-total cloud cover and relatively high longwave optical depths, their effective emission temperature is governed by the fact that deep tropical anvils, despite rising with warming, remain at a nearly fixed temperature. These two factors produce a mean-state atmosphere with a nearly warming-independent minimum outgoing longwave heating anomaly, which thus cannot effectively compensate for increases in MJO-scale convective activity and precipitation.

Our moisture budget analysis also revealed that MJO strengthening occurs in part due to changes in the meridional moisture advection term, which is consistent with previous work. For example, Wang et al. (2025) found an increased contribution from meridional advection with warming across multiple CMIP6 models, though in that study the meridional advection acted as a moistening factor in both present and future climates. Our results, by contrast, indicate that meridional moisture advection acts to dampen MJO activity such that increased MJO growth with warming results from a less negative meridional moisture term in a warmer climate. In decomposing the meridional advection term by timescale, Wang et al. (2025) also found the two dominant terms to be advection of mean moisture by the MJO scale winds and modulation of high-frequency eddy activity, the major difference between their study and ours being that high-frequency eddy activity in their work acted to moisten the MJO as opposed to the drying effect reported here. One potential source of such a discrepancy may be the absence of both land and zonal asymmetries in the present study, with the presence of the Maritime Continent in particular affecting the meridional moisture gradient. We also highlight the increased moistening with warming induced by the advection of MJO-scale moisture by the mean meridional winds, which transition from damping the MJO in the -4K simulation to weakly amplifying it in the +4K simulation. Physically, this transition occurs as regions of moistening become more in-phase with the MJO's positive moisture anomaly with warming, though the underlying cause of this changing zonal phase relationship merits further research.

Acknowledgments. We acknowledge support from NOAA MAPP program grant NA21OAR4310343, NOAA CVP program grant NA22OAR4310608,and NASA MAP program grant 80NSSC21K1495. SR was supported by the National Science Foundation Graduate Research Fellowship Program. DK was also supported by the Creative-Pioneering Researchers Program from Seoul National University, the National Research Foundation of Korea (NRF) grant funded by the Korea government (MSIT) (RS-2024-00336160), and the Korea Meteorological Administration Research and Development Program under Grant (RS-2025-02221669).

Data availability statement. The simulation data and code used in this work can be found at the following DOI: https://doi.org/10.5281/zenodo.21796859

References

Abhik, S., and H. H. Hendon, 2019: Influence of the QBO on the MJO During Coupled Model Multiweek Forecasts. *Geophysical Research Letters*, **46 (15)**, 9213–9221, https://doi.org/10.1029/2019GL083152.

Adames, Á. F., and D. Kim, 2016: The MJO as a Dispersive, Convectively Coupled Moisture Wave: Theory and Observations. *Journal of the Atmospheric Sciences*, **73 (3)**, 913–941, https://doi.org/10.1175/JAS-D-15-0170.1.

Adames, Á. F., D. Kim, A. H. Sobel, A. Del Genio, and J. Wu, 2017: Changes in the structure and propagation of the MJO with increasing CO2. *Journal of Advances in Modeling Earth Systems*, **9 (2)**, 1251–1268, https://doi.org/10.1002/2017MS000913.

Ahmed, F., 2021: The MJO on the Equatorial Beta Plane: An Eastward-Propagating Rossby Wave Induced by Meridional Moisture Advection. *Journal of the Atmospheric Sciences*, **78 (10)**, 3115–3135, https://doi.org/10.1175/JAS-D-21-0071.1.

Alvarez, M. S., C. S. Vera, G. N. Kiladis, and B. Liebmann, 2016: Influence of the Madden Julian Oscillation on precipitation and surface air temperature in South America. *Climate Dynamics*, **46 (1)**, 245–262, https://doi.org/10.1007/s00382-015-2581-6.

Andersen, J. A., and Z. Kuang, 2012: Moist Static Energy Budget of MJO-like Disturbances in the Atmosphere of a Zonally Symmetric Aquaplanet. *Journal of Climate*, **25 (8)**, 2782–2804, https://doi.org/10.1175/JCLI-D-11-00168.1.

Arnold, N. P., M. Branson, Z. Kuang, D. A. Randall, and E. Tziperman, 2015: MJO Intensification with Warming in the Superparameterized CESM. *Journal of Climate*, https://doi.org/10.1175/JCLI-D-14-00494.1.

Arnold, N. P., Z. Kuang, and E. Tziperman, 2013: Enhanced MJO-like Variability at High SST. *Journal of Climate*, https://doi.org/10.1175/JCLI-D-12-00272.1.

Arnold, N. P., and D. A. Randall, 2015: Global-scale convective aggregation: Implications for the Madden-Julian Oscillation. *Journal of Advances in Modeling Earth Systems*, **7 (4)**, 1499–1518, https://doi.org/10.1002/2015MS000498.

Benedict, J. J., E. D. Maloney, A. H. Sobel, and D. M. W. Frierson, 2014: Gross Moist Stability and MJO Simulation Skill in Three Full-Physics GCMs. *Journal of the Atmospheric Sciences*, **71 (9)**, 3327–3349, https://doi.org/10.1175/JAS-D-13-0240.1.

Bui, H. X., Y.-X. Li, E. D. Maloney, J.-E. Kim, S.-S. Lee, and J.-Y. Yu, 2023: Emergence of Madden-Julian oscillation precipitation and wind amplitude changes in a warming climate. *npj Climate and Atmospheric Science*, **6 (1)**, 22, https://doi.org/10.1038/s41612-023-00344-z.

Bui, H. X., and E. D. Maloney, 2018: Changes in Madden-Julian Oscillation Precipitation and Wind Variance Under Global Warming. *Geophysical Research Letters*, **45 (14)**, 7148–7155, https://doi.org/10.1029/2018GL078504.

Carlson, H., and R. Caballero, 2016: Enhanced MJO and transition to superrotation in warm climates. *Journal of Advances in Modeling Earth Systems*, **8 (1)**, 304–318, https://doi.org/10.1002/2015MS000615.

Chien, M.-T., and D. Kim, 2024: Response of Convectively Coupled Kelvin Waves to Surface Temperature Forcing in Aquaplanet Simulations. *Journal of Advances in Modeling Earth Systems*, **16 (10)**, e2024MS004 378, https://doi.org/10.1029/2024MS004378.

Chikira, M., 2014: Eastward-Propagating Intraseasonal Oscillation Represented by Chikira–Sugiyama Cumulus Parameterization. Part II: Understanding Moisture Variation under Weak Temperature Gradient Balance. *Journal of the Atmospheric Sciences*, **71 (2)**, 615–639, https://doi.org/10.1175/JAS-D-13-038.1.

Chou, C., T.-C. Wu, and P.-H. Tan, 2013: Changes in gross moist stability in the tropics under global warming. *Climate Dynamics*, **41 (9)**, 2481–2496, https://doi.org/10.1007/s00382-013-1703-2.

Danabasoglu, G., and Coauthors, 2020: The Community Earth System Model Version 2 (CESM2). *Journal of Advances in Modeling Earth Systems*, **12 (2)**, e2019MS001 916, https://doi.org/10.1029/2019MS001916.

Del Genio, A. D., and Y. Chen, 2015: Cloud-radiative driving of the Madden-Julian oscillation as seen by the A-Train. *Journal of Geophysical Research: Atmospheres*, **120 (11)**, 5344–5356, https://doi.org/10.1002/2015JD023278.

DeMott, C. A., N. P. Klingaman, and S. J. Woolnough, 2015: Atmosphere-ocean coupled processes in the Madden-Julian oscillation. *Reviews of Geophysics*, **53 (4)**, 1099–1154, https://doi.org/10.1002/2014RG000478.

Emlaw, G. N., and D. Kim, 2024: The Role of Precursor Disturbances on the Modulation of Western Pacific Tropical Cyclogenesis by the Madden-Julian Oscillation. *Geophysical Research Letters*, **51 (12)**, e2023GL108 102, https://doi.org/10.1029/2023GL108102.

Frierson, D. M. W., 2006: Robust increases in midlatitude static stability in simulations of global warming. *Geophysical Research Letters*, **33 (24)**, https://doi.org/10.1029/2006GL027504.

Gill, A. E., 1980: Some simple solutions for heat-induced tropical circulation. *Quarterly Journal of the Royal Meteorological Society*, **106 (449)**, 447–462, https://doi.org/10.1002/qj.49710644905.

Grimm, A. M., 2019: Madden–Julian Oscillation impacts on South American summer monsoon season: Precipitation anomalies, extreme events, teleconnections, and role in the MJO cycle. *Climate Dynamics*, **53 (1)**, 907–932, https://doi.org/10.1007/s00382-019-04622-6.

Hartmann, D. L., and K. Larson, 2002: An important constraint on tropical cloud - climate feedback. *Geophysical Research Letters*, **29 (20)**, 12–1–12–4, https://doi.org/10.1029/2002GL015835.

Held, I. M., and B. J. Soden, 2006: Robust Responses of the Hydrological Cycle to Global Warming. *Journal of Climate*, https://doi.org/10.1175/JCLI3990.1.

Henderson, S. A., E. D. Maloney, and E. A. Barnes, 2016: The Influence of the Madden–Julian Oscillation on Northern Hemisphere Winter Blocking. *Journal of Climate*, **29 (12)**, 4597–4616, https://doi.org/10.1175/JCLI-D-15-0502.1.

Hendon, H. H., and M. L. Salby, 1994: The Life Cycle of the Madden–Julian Oscillation. *Journal of the Atmospheric Sciences*, **51 (15)**, 2225–2237, https://doi.org/10.1175/1520-0469(1994)051⟨2225:TLCOTM⟩2.0.CO;2.

Hersbach, H., and Coauthors, 2020: The ERA5 global reanalysis. *Quarterly Journal of the Royal Meteorological Society*, **146 (730)**, 1999–2049, https://doi.org/10.1002/qj.3803.

Hidayat, R., and S. Kizu, 2010: Influence of the Madden–Julian Oscillation on Indonesian rainfall variability in austral summer. *International Journal of Climatology*, **30 (12)**, 1816–1825, https://doi.org/10.1002/joc.2005.

Inoue, K., and L. Back, 2015: Column-Integrated Moist Static Energy Budget Analysis on Various Time Scales during TOGA COARE. *Journal of the Atmospheric Sciences*, **72 (5)**, 1856–1871, https://doi.org/10.1175/JAS-D-14-0249.1.

Jia, X., L. Chen, F. Ren, and C. Li, 2011: Impacts of the MJO on winter rainfall and circulation in China. *Advances in Atmospheric Sciences*, **28 (3)**, 521–533, https://doi.org/10.1007/s00376-010-9118-z.

Kang, W., and E. Tziperman, 2018: The MJO-SSW Teleconnection: Interaction Between MJO-Forced Waves and the Midlatitude Jet. *Geophysical Research Letters*, **45 (9)**, 4400–4409, https://doi.org/10.1029/2018GL077937.

Kessler, W. S., 2001: EOF Representations of the Madden–Julian Oscillation and Its Connection with ENSO. *Journal of Climate*.

Kim, D., M.-S. Ahn, I.-S. Kang, and A. D. D. Genio, 2015: Role of Longwave Cloud–Radiation Feedback in the Simulation of the Madden–Julian Oscillation. *Journal of Climate*, **28 (17)**, 6979–6994, https://doi.org/10.1175/JCLI-D-14-00767.1.

Kim, H.-M., P. J. Webster, V. E. Toma, and D. Kim, 2014: Predictability and Prediction Skill of the MJO in Two Operational Forecasting Systems. *Journal of Climate*, https://doi.org/10.1175/JCLI-D-13-00480.1.

Kim, S., J.-S. Kug, and K.-H. Seo, 2020: Impacts of MJO on the Intraseasonal Temperature Variation in East Asia. *Journal of Climate*, https://doi.org/10.1175/JCLI-D-20-0302.1.

Klotzbach, P. J., and E. C. J. Oliver, 2015: Modulation of Atlantic Basin Tropical Cyclone Activity by the Madden–Julian Oscillation (MJO) from 1905 to 2011. *Journal of Climate*, https://doi.org/10.1175/JCLI-D-14-00509.1.

Lee, H.-J., and K.-H. Seo, 2019: Impact of the Madden-Julian oscillation on Antarctic sea ice and its dynamical mechanism. *Scientific Reports*, **9 (1)**, 10 761, https://doi.org/10.1038/s41598-019-47150-3.

Liu, P., 2013: Changes in a modeled MJO with idealized global warming. *Climate Dynamics*, **40 (3)**, 761–773, https://doi.org/10.1007/s00382-012-1323-2.

Lorenz, D. J., and D. L. Hartmann, 2006: The Effect of the MJO on the North American Monsoon. *Journal of Climate*, **19 (3)**, 333–343, https://doi.org/10.1175/JCLI3684.1.

Madden, R. A., and P. R. Julian, 1971: Detection of a 40–50 Day Oscillation in the Zonal Wind in the Tropical Pacific. *Journal of the Atmospheric Sciences*, **28 (5)**, 702–708, https://doi.org/10.1175/1520-0469(1971)028⟨0702:DOADOI⟩2.0.CO;2.

Madden, R. A., and P. R. Julian, 1972: Description of Global-Scale Circulation Cells in the Tropics with a 40–50 Day Period. *Journal of the Atmospheric Sciences*, **29 (6)**, 1109–1123, https://doi.org/10.1175/1520-0469(1972)029⟨1109:DOGSCC⟩2.0.CO;2.

Maloney, E. D., and D. L. Hartmann, 2000a: Modulation of Eastern North Pacific Hurricanes by the Madden–Julian Oscillation. *Journal of Climate*, **13 (9)**, 1451–1460, https://doi.org/10.1175/1520-0442(2000)013⟨1451:MOENPH⟩2.0.CO;2.

Maloney, E. D., and D. L. Hartmann, 2000b: Modulation of Hurricane Activity in the Gulf of Mexico by the Madden-Julian Oscillation. *Science*, **287 (5460)**, 2002–2004, https://doi.org/10.1126/science.287.5460.2002.

Mapes, B., S. Tulich, J. Lin, and P. Zuidema, 2006: The mesoscale convection life cycle: Building block or prototype for large-scale tropical waves? *Dynamics of Atmospheres and Oceans*, **42 (1)**, 3–29, https://doi.org/10.1016/j.dynatmoce.2006.03.003.

Marshall, A. G., H. H. Hendon, D. Hudson, A. G. Marshall, H. H. Hendon, and D. Hudson, 2021: Influence of the Madden-Julian Oscillation on multiweek prediction of Australian rainfall extremes using the ACCESS-S1 prediction system. *Journal of Southern Hemisphere Earth Systems Science*, **71 (2)**, 159–180, https://doi.org/10.1071/ES21001.

Matus, F., R. Rondanelli, J. Rutllant, and S. Henderson, 2025: Mechanisms for the Influence of the MJO on Precipitation in Southwestern South America. *Journal of Geophysical Research: Atmospheres*, **130 (1)**, e2024JD041 935, https://doi.org/10.1029/2024JD041935.

Neale, R. B., and B. J. Hoskins, 2000: A standard test for AGCMs including their physical parametrizations: I: The proposal. *Atmospheric Science Letters*, **1 (2)**, 101–107, https://doi.org/10.1006/asle.2000.0019.

Neelin, J. D., I. M. Held, and K. H. Cook, 1987: Evaporation-Wind Feedback and Low-Frequency Variability in the Tropical Atmosphere. *Journal of the Atmospheric Sciences*, **44 (16)**, 2341–2348, https://doi.org/10.1175/1520-0469(1987)044⟨2341:EWFALF⟩2.0.CO;2.

Oliver, E. C. J., and K. R. Thompson, 2011: A Reconstruction of Madden–Julian Oscillation Variability from 1905 to 2008. *Journal of Climate*, https://doi.org/10.1175/JCLI-D-11-00154.1.

Pai, D. S., J. Bhate, O. P. Sreejith, and H. R. Hatwar, 2011: Impact of MJO on the intraseasonal variation of summer monsoon rainfall over India. *Climate Dynamics*, **36 (1)**, 41–55, https://doi.org/10.1007/s00382-009-0634-4.

Peters, M. E., and C. S. Bretherton, 2005: A Simplified Model of the Walker Circulation with an Interactive Ocean Mixed Layer and Cloud-Radiative Feedbacks. *Journal of Climate*, **18 (20)**, 4216–4234, https://doi.org/10.1175/JCLI3534.1.

Pritchard, M. S., and D. Yang, 2016: Response of the Superparameterized Madden–Julian Oscillation to Extreme Climate and Basic-State Variation Challenges a Moisture Mode View. *Journal of Climate*, https://doi.org/10.1175/JCLI-D-15-0790.1.

Raymond, D. J., S. L. Sessions, A. H. Sobel, and Ž. Fuchs, 2009: The Mechanics of Gross Moist Stability. *Journal of Advances in Modeling Earth Systems*, **1 (3)**, https://doi.org/10.3894/james.2009.1.9.

Ren, P., D. Kim, M.-S. Ahn, D. Kang, and H.-L. Ren, 2021: Intercomparison of MJO Column Moist Static Energy and Water Vapor Budget among Six Modern Reanalysis Products. *Journal of Climate*, https://doi.org/10.1175/JCLI-D-20-0653.1.

Riddle, E. E., M. B. Stoner, N. C. Johnson, M. L. L'Heureux, D. C. Collins, and S. B. Feldstein, 2013: The impact of the MJO on clusters of wintertime circulation anomalies over the North American region. *Climate Dynamics*, **40 (7)**, 1749–1766, https://doi.org/10.1007/s00382-012-1493-y.

Roundy, P. E., 2008: Analysis of Convectively Coupled Kelvin Waves in the Indian Ocean MJO. *Journal of the Atmospheric Sciences*, https://doi.org/10.1175/2007JAS2345.1.

Rushley, S. S., D. Kim, and Á. F. Adames, 2019: Changes in the MJO under Greenhouse Gas–Induced Warming in CMIP5 Models. *Journal of Climate*, https://doi.org/10.1175/JCLI-D-18-0437.1.

Sakaeda, N., J. Dias, and G. N. Kiladis, 2020: The Unique Characteristics and Potential Mechanisms of the MJO-QBO Relationship. *Journal of Geophysical Research: Atmospheres*, **125 (17)**, e2020JD033 196, https://doi.org/10.1029/2020JD033196.

Seo, K.-H., H.-J. Lee, and D. M. W. Frierson, 2016: Unraveling the Teleconnection Mechanisms that Induce Wintertime Temperature Anomalies over the Northern Hemisphere Continents in Response to the MJO. *Journal of the Atmospheric Sciences*, https://doi.org/10.1175/JAS-D-16-0036.1.

Sobel, A., S. Wang, and D. Kim, 2014: Moist Static Energy Budget of the MJO during DYNAMO. *Journal of the Atmospheric Sciences*, **71 (11)**, 4276–4291, https://doi.org/10.1175/JAS-D-14-0052.1.

Sobel, A. H., J. Nilsson, and L. M. Polvani, 2001: The Weak Temperature Gradient Approximation and Balanced Tropical Moisture Waves. *Journal of the Atmospheric Sciences*, **58 (23)**, 3650–3665, https://doi.org/10.1175/1520-0469(2001)058⟨3650:TWTGAA⟩2.0.CO;2.

Subramanian, A., M. Jochum, A. J. Miller, R. Neale, H. Seo, D. Waliser, and R. Murtugudde, 2014: The MJO and global warming: A study in CCSM4. *Climate Dynamics*, **42 (7)**, 2019–2031, https://doi.org/10.1007/s00382-013-1846-1.

Tao, L., J. Zhao, and T. Li, 2015: Trend analysis of tropical intraseasonal oscillations in the summer and winter during 1982–2009. *International Journal of Climatology*, **35 (13)**, 3969–3978, https://doi.org/10.1002/joc.4258.

Tippett, M. K., 2018: Robustness of Relations between the MJO and U.S. Tornado Occurrence. *Monthly Weather Review*, https://doi.org/10.1175/MWR-D-18-0207.1.

Vecchi, G. A., and N. A. Bond, 2004: The Madden-Julian Oscillation (MJO) and northern high latitude wintertime surface air temperatures. *Geophysical Research Letters*, **31 (4)**, https://doi.org/10.1029/2003GL018645.

Waliser, D. E., K. M. Lau, W. Stern, and C. Jones, 2003: Potential Predictability of the Madden–Julian Oscillation. *Bulletin of the American Meteorological Society*, **84 (1)**, 33–50, https://doi.org/10.1175/BAMS-84-1-33.

Wang, J., M. J. DeFlorio, H. Kim, K. Guirguis, and A. Gershunov, 2025: Future MJO Change and Its Impact on Extreme Precipitation and Temperature Over the Western US in CMIP6. *Journal of Geophysical Research: Atmospheres*, **130 (5)**, e2024JD042 123, https://doi.org/10.1029/2024JD042123.

Wheeler, M., and G. N. Kiladis, 1999: Convectively Coupled Equatorial Waves: Analysis of Clouds and Temperature in the Wavenumber–Frequency Domain. *Journal of the Atmospheric Sciences*, **56 (3)**, 374–399, https://doi.org/10.1175/1520-0469(1999)056⟨0374:CCEWAO⟩2.0.CO;2.

Wheeler, M. C., and H. H. Hendon, 2004: An All-Season Real-Time Multivariate MJO Index: Development of an Index for Monitoring and Prediction. *Monthly Weather Review*, **132 (8)**, 1917–1932, https://doi.org/10.1175/1520-0493(2004)132⟨1917:AARMMI⟩2.0.CO;2.

Wheeler, M. C., H. H. Hendon, S. Cleland, H. Meinke, and A. Donald, 2009: Impacts of the Madden–Julian Oscillation on Australian Rainfall and Circulation. *Journal of Climate*, **22 (6)**, 1482–1498, https://doi.org/10.1175/2008JCLI2595.1.

Wolding, B. O., E. D. Maloney, S. Henderson, and M. Branson, 2017: Climate change and the Madden-Julian Oscillation: A vertically resolved weak temperature gradient analysis. *Journal of Advances in Modeling Earth Systems*, **9 (1)**, 307–331, https://doi.org/10.1002/2016MS000843.

Xu, K.-M., and K. A. Emanuel, 1989: Is the Tropical Atmosphere Conditionally Unstable? *Monthly Weather Review*, **117 (7)**, 1471–1479, https://doi.org/10.1175/1520-0493(1989)117⟨1471:ITTACU⟩2.0.CO;2.